ARL

US Army Research Laboratory

Simulation of Blast on Porcine Head

by Yolin Huang

NOTICES

Disclaimers

The findings in this report are not to be construed as an official Department of the Army position unless so designated by other authorized documents.

Citation of manufacturer's or trade names does not constitute an official endorsement or approval of the use thereof.

Destroy this report when it is no longer needed. Do not return it to the originator.

US Army Research Laboratory

Simulation of Blast on Porcine Head

by Yolin Huang
Weapons and Materials Research Directorate, ARL

REPORT DOCUMENTATION PAGE		*Form Approved* *OMB No. 0704-0188*

Public reporting burden for this collection of information is estimated to average 1 hour per response, including the time for reviewing instructions, searching existing data sources, gathering and maintaining the data needed, and completing and reviewing the collection information. Send comments regarding this burden estimate or any other aspect of this collection of information, including suggestions for reducing the burden, to Department of Defense, Washington Headquarters Services, Directorate for Information Operations and Reports (0704-0188), 1215 Jefferson Davis Highway, Suite 1204, Arlington, VA 22202-4302. Respondents should be aware that notwithstanding any other provision of law, no person shall be subject to any penalty for failing to comply with a collection of information if it does not display a currently valid OMB control number.
PLEASE DO NOT RETURN YOUR FORM TO THE ABOVE ADDRESS.

1. REPORT DATE *(DD-MM-YYYY)*	2. REPORT TYPE	3. DATES COVERED (From - To)
July 2015	Final	January 2013–May 2015

4. TITLE AND SUBTITLE	5a. CONTRACT NUMBER
Simulation of Blast on Porcine Head	
	5b. GRANT NUMBER
	5c. PROGRAM ELEMENT NUMBER
6. AUTHOR(S)	5d. PROJECT NUMBER
Yolin Huang	H80
	5e. TASK NUMBER
	5f. WORK UNIT NUMBER

7. PERFORMING ORGANIZATION NAME(S) AND ADDRESS(ES)	8. PERFORMING ORGANIZATION REPORT NUMBER
US Army Research Laboratory ATTN: RDRL-WMP-B Aberdeen Proving Ground, MD 21005	ARL-TR-7340

9. SPONSORING/MONITORING AGENCY NAME(S) AND ADDRESS(ES)	10. SPONSOR/MONITOR'S ACRONYM(S)
	11. SPONSOR/MONITOR'S REPORT NUMBER(S)

12. DISTRIBUTION/AVAILABILITY STATEMENT
Approved for public release; distribution is unlimited.

13. SUPPLEMENTARY NOTES

14. ABSTRACT
Shock tube blast on porcine head experimental data, including incident pressure, surface pressure, intracranial pressure, and cranial acceleration, has been compared with simulation using ALE3D. Other physical variables (coup-contrecoup pressure profile, vaporization pressure, skull strain, strain in brain, effective stress, deviatoric strain energy, Löwenhielm vein injury criterion, viscous injury criterion, linear acceleration, and angular acceleration) in the simulations do not have corresponding test data for comparison; they are discussed in association with their injury instigation implications with references to other published findings. The effect of variation of shear modulus based on published measurement data for the brain on impact response is discussed. Furthermore, some nuances about the shock tube simulation are discussed. With progress in geometry-conforming meshing technique, in noninvasive high-rate properties, and in development in material models, further advances in simulation fidelity will emerge. They will help in early diagnosis, treatment, and prevention of brain injury.

15. SUBJECT TERMS
traumatic brain injury, TBI, blast head pig, ALE3D, simulation

16. SECURITY CLASSIFICATION OF:			17. LIMITATION OF ABSTRACT	18. NUMBER OF PAGES	19a. NAME OF RESPONSIBLE PERSON
			UU	76	Yolin Huang
a. REPORT	b. ABSTRACT	c. THIS PAGE			19b. TELEPHONE NUMBER (Include area code)
Unclassified	Unclassified	Unclassified			410-278-6859

Standard Form 298 (Rev. 8/98)
Prescribed by ANSI Std. Z39.18

Contents

List of Figures

List of Tables

Acknowledgments

1. Introduction

Explosive blast accounts for over 63% of combat casualties, and 20% of the deployed force potentially suffer from traumatic brain injury (TBI) (DePalma et al. 2005; Hoge et al. 2008; Ling et al. 2009; Rosenfeld and Ford 2010; Theeler and Jackson 2012). Bomb blasts accounts for 82% of all injuries caused by terrorists worldwide (Champion et al. 2009; Covey and Born 2010; Capehart and Bass 2012). To find mitigation countermeasures and treatment methods (Margulies et al. 2009), the shock tube is a frequently used lab tool. The shock tube provides controllable and a repeatable shock pressure wave (Richmond and White 1966; Martinez 1999; Bauman et al. 2009; Long et al. 2010; Kleinschmit 2011; Stuhmiller 2011; Varas 2011; Panzer 2012; Reneer 2012; Zhu et al. 2012; Courtney et al. 2014). Shock tubes of various cross-sectional sizes and shapes and various tube lengths have been designed for tests on assorted vehicles, equipment, and animals large and small.

Animals tested include mice, rats, hamsters, guinea pigs, rabbits, cats, dogs, goats, sheep, burros, swine, monkeys, and cattle for tests to find eardrum failure threshold, lung damage threshold, and lethality threshold. Scaling models have been developed to find a survivable over-pressure range from test data with animals (Bowen et al. 1968; Bass et al. 2008; Courtney et al. 2011; Panzer et al. 2011; Jean et al. 2014). Using animal models to study brain injury, the characteristics of the brain anatomy need to be considered. Among the animals tested, the porcine brain has unique characteristics: It is gyrencephalic with a gyrification index similar to that of the human brain (Neal et al. 2007; Zilles et al. 2013; Lewitus et al. 2014). The porcine gray matter to white matter ratio is also similar to the human ratio (Zhang and Sejnowski 2000; Bush 2003; Winter 2011). Therefore, animal models with porcine brains should have greater relevancy to the human brain injury research (Finnie and Blumberg 2002; Cernak 2005; Manley et al. 2005; Swindle et al. 2012).

A series of experiments applying a blast wave from a shock tube for pressure loading on porcine heads has been conducted at Duke University (Shridharani 2012). This report describes the simulation work to study the porcine head response. The simulation uses the ALE3D code (LLNL 2014). In the following sections, the material models are discussed first, then the mesh setup for the simulations, followed by the simulation results for comparison, and finally other calculated physical quantities are presented. The objective is to attain insight into the experiments conducted at Duke University and understand the loading associated with blast-related brain injury mechanics.

2. Material Models

2.1 Soft Tissue

A newly implemented, compressible version of the Mooney-Rivlin model (Becker 2014) is used for soft tissue. This nonlinear hyperelastic model is not tied to any particular equation of state; any equation of state in the ALE3D package for the pressure may be used. The constitutive relation for the deviatoric part, **S**, of the Cauchy stress tensor is given by

$$\mathbf{S} = \frac{\mu_0}{J}\big[\omega_0 \, dev\widetilde{\mathbf{B}} - (1 - \omega_0)dev(\widetilde{\mathbf{B}}^{-1})\big], \tag{1}$$

where $\widetilde{\mathbf{B}} = \mathbf{B}/J^{2/3}$ is the volume adjusted part of the left Cauchy-Green deformation tensor $\mathbf{B} = \mathbf{FF}^T$, *dev* denotes the deviatoric part, **F** denotes the deformation gradient, $J = \det \mathbf{F} = (\det \mathbf{B})^{1/2}$ is the Jacobian, μ_0 is the shear modulus at small strains, and ω_0 is a dimensionless constant with $0 < \omega_0 \leq 1$. This new model eliminates the complicated and physically unrealistic features of the compressible Mooney-Rivlin model originally in ALE3D (and currently in LS-DYNA); (cf. the discussion in Appendix A of Scheidler [2010]). The relationships between the parameters μ_0 and ω_0 above and the parameters A and B in the previous model (ALE3D ysmodel 144) are $A = \frac{1}{2}\omega_0\mu_0$ and $B = \frac{1}{2}(1 - \omega_0)\mu_0$. The accuracy of the advection of **B** is enhanced by advecting the logarithm of **B**.

For this new version of the Mooney-Rivlin model (ALE3D ysmodel 146), the axial stress σ in a uniaxial stress test is given by

$$\sigma = \frac{\mu_0}{J}\Big[\omega_0\Big(\lambda^2 - \frac{1}{\lambda}\Big) - (1 - \omega_0)\Big(\frac{1}{\lambda^2} - \lambda\Big)\Big], \tag{2}$$

where λ is the principal stretch in axial direction with the isochoric deformation assumption. The pressure was determined by setting the lateral stress to zero. For a nearly incompressible material like soft tissue, the Jacobian J may be set to 1 in Eq. 2, since the volume change in a uniaxial stress test will be negligible.

Quasi-static uniaxial stress data at strain rates from 10^{-3}/s to 1/s was available for soft tissue. Due to lack of reliable data at the higher strain rates generated by projectile penetration, the quasi-static data was qualitatively extrapolated to yield a stress-stretch curve for strain rates of 10^3–10^4/s. The model is rate-independent. A fit is constructed at a strain rate of 10^3–10^4/s to produce stresses consistent with deformation at the higher rates. Equation 2 (J = 1) was then fit to this extrapolated

curve (Scheidler 2010), giving $\mu_0 = 80$ kPa (0.8 bar) and $\omega_0 = 0.3$. This value of the shear modulus is within the range of values found in the literature: 4.2–23.0 psi (or 0.289–1.59 bar) (Winter 1975).

The Grüneisen form of the equation of state (as implemented in ALE3D) is used for the ballistic gelatin as follows:

$$P = \frac{\rho_0 c^2 K \left[1 + \left(1 - \frac{\gamma_0}{2}\right)K - \frac{a}{2}K^2\right]}{\left[1 - (S_1 - 1)K - S_2\frac{K^2}{(K+1)} - S_3\frac{K^3}{(K+1)^2}\right]^2} + (\gamma_0 + aK)e, \tag{3}$$

where the compression K is given by $K = \left(\frac{\rho}{\rho_0} - 1\right)$; S_1, S_2, and S_3 are coefficients from the $U_S - u_p$ relationship; and γ_0 is the Grüneisen parameter.

The reference density, ρ_0, is 1.05 g/cm^3 (Winter 1975). The bulk sound speed, c, is 0.156 cm/µs. The bulk modulus is 0.026 Mbar. The cubic polynomial coefficients fitting the shock compression curve are the same as those for water: $S_1 = 2.56$, $S_2 = -1.986$, $S_3 = 0.2268$; the Grüneisen parameter γ_0 is constant 0.5 and the linear correction factor, a, is 0.

2.2 Brain

The Mooney-Rivlin model is also applied for the brain. The density of the brain is chosen to be 1.04 g/cm^3 (Claessens et al. 1997; Wang et al. 2007; Ho and Kleiven 2009; Watanabe et al. 2009). The bulk modulus is set to be 2.19 GPa (0.022 Mbar) (Margulies and Meany 1998; Zong et al. 2006; Watanabe et al. 2009). The bulk sound speed (calculated from the bulk modulus and density) is 0.145 cm/µs. The shear modulus, μ_0, is 13 kPa and $\omega_0 = 0$ (Ott et al. 2012). The Poisson's ratio calculated from the bulk and shear moduli is 0.4999. The cubic polynomial coefficients fitting the shock compression curve are the same as those for water: $S_1 = 2.56$, $S_2 = -1.986$, and $S_3 = 0.2268$; the Grüneisen parameter γ_0 is constant 0.5 and the linear correction factor, a, is 0.

2.3 Skull

The density of the skull is chosen to be 1.412 g/cm^3 (Sauren and Claessens 1993; Henry and Letowski 2007; Moore et al. 2009; Taylor et al. 2009). This number came from earlier measurements with human cadaver skulls, 0.051 lb/in^3 (1.412 g/cm^3) (McElhaney 1970). The material is modeled as homogenous (i.e., with no distinction between the skull and the suture). Density fractionation measurement with the porcine cortical bone powder samples shows that about 65% of dry bone powder has density values in the 2.0- to 2.1-g/mL range and about 30% is in the 2.1- to 2.2-g/mL range, while for human bone powder, about 80% is in the 2.0- to

3

2.1-g/mL range and about 15% is in the 2.1- to 2.2-g/mL range (Aerssens et al. 1998). However, this density was measured from the dry bone powder prepared from femoral shaft bone samples. The skull, being porous, would have a lower density than the measured values. The Young's modulus is set to 6.5 GPa (Moore et al. 2009; Motherway et al. 2009; Taylor et al. 2009). Poisson's ratio is set to 0.22. The elastic model is applied to model the skull.

The material parameters are summarized in Tables 1–3.

Table 1   Material parameters in the model

Sample	Density (g/cm^3)	Shear Modulus	ω_0	Bulk Modulus (Mbar)
Soft tissue	1.05	0.8 bar	0.3	0.026
Brain	1.04	0.13 bar	0	0.022
Skull	1.412	0.026 Mbar	. . .	0.038

Table 2   Derived variables

Sample	Bulk Sound Speed (cm/μs)	Young's Modulus	Poisson Ratio
Soft tissue	0.156	240 kPa	0.4999
Brain	0.145	39 kPa	0.4999
Skull	0.165	6.5 GPa	0.22

Table 3   Coefficients for the Grüneisen form of the equation of state

Sample	S_1	S_2	S_3	γ_0	a
Soft tissue	2.56	–1.986	0.2268	0.5	0
Brain	2.56	–1.986	0.2268	0.5	0
Skull	0.94	0	0	1.0	0

3.   The Simulation Setup

Since the recorded pressure history at the exit of the shock tube is not sufficient for use as boundary condition to drive the simulation, to accurately simulate the blast from the shock tube, the whole shock tube has to be modelled. In the experiments the shock tube has a 12-inch (30.5-cm) driver section where nitrogen is used as the driver medium. The driven section is 10-ft (304.8-cm) long with a 12-inch diameter (Fig. 1). Flush-mounted pressure transducers located 1/4-inch inward from the tube exit record the pressure trace near the exit (Endevco 8530B, San Juan Capistrano, CA) (Shridharani 2012).
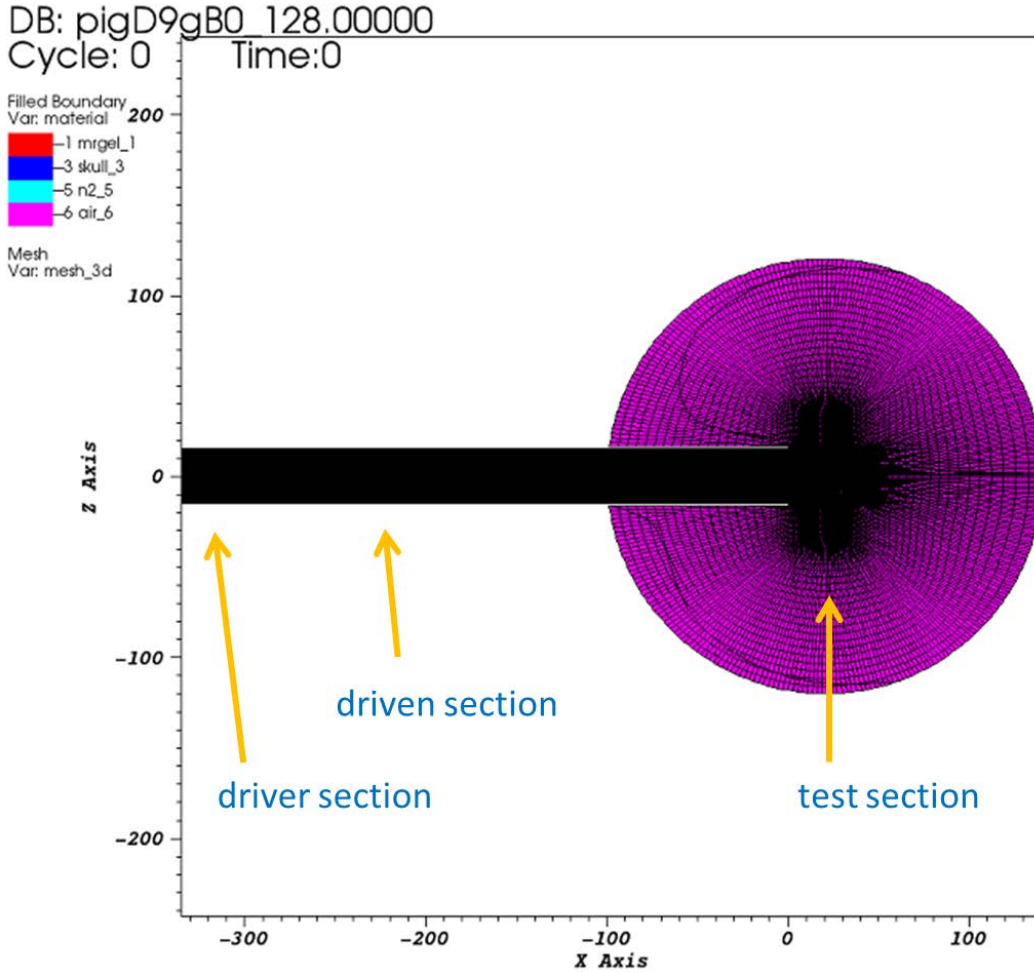
Fig. 1   Mesh configuration for the shock tube and the space around the test object

Within the shock tube, the mesh is advection-enabled during simulation. The mesh element size is initially around (X × Y × Z) = 0.6 × 0.5 × 0.5 cm or less. With weighted advection, the mesh element size can reduce to around (X × Y × Z) = 0.4 × 0.5 × 0.5 cm or less near the shock front during the passage of the shock front.

For the object space (the space directly outside the tube exit, where the test object is placed) the mesh stays Eulerian; 2 meshes, 1 finer and 1 coarser, have been used for this report. With the finer mesh, the mesh element is about 0.3 × 0.2 × 0.2 cm around the test object, while with the coarser mesh, the mesh elements having dimensions about 0.6 × 0.5 × 0.5 cm around the test object, is run for comparison.

In the region further downstream of the test object, the mesh needs to be extended far enough such that the pressure profile at the downstream boundary should not affect the computational accuracy near the center of the simulation (the space just outside the tube exit). Beyond the tube exit, the mesh is extended by 140 cm in the

5

axial X direction and 120 cm in the radial direction (Y or Z). The mesh element size increases gradually both in the X direction and in the radial direction away from the core region with constant-sized mesh (Fig. 1).

The porcine head is created from computed tomography (CT) images of a porcine head, which is different from the one used in the blast tests (Yorkshire pigs). The solid volume for the porcine head is shaped into the ALE3D mesh. Since only the head portion is digitally available, the cervical spine is numerically fixed to the coordinates to emulate the presence of the porcine body.

4. Comparison with Experimental Data

The simulations with ALE3D use centimeters, microseconds, grams, and megabar (the B-Division units) (LLNL 2014), in which the pressure uses megabar for simulation; 1 Mbar = 10^5 MPa.

4.1 Comparison with Measured Pressure Trace near the Tube Exit

In the experiments the blast gas flow in the shock tube is characterized only by the pressure measured near the exit of the shock tube with transducers at 1/4-inch upstream of the tube exit, evenly spaced around the tube circumference (Shridharani 2012). One such pressure trace dataset for an incident pressure of 2.6 bar gauge (37.7 psig) has been provided by the experimentalist group. However, the pressure in the driver section of the shock tube is not provided by the experimentalists. Instead the pressure in the driver section is estimated with the analytical relationship for pressures of a 1-dimensional (1-D) Riemann shock tube problem, as follows:

$$\frac{p_3}{p_1} = \frac{p_2}{p_1}\left[1 - (\gamma - 1)\frac{\frac{p_2}{p_1}-1}{\sqrt{2\gamma\left[(\gamma+1)\frac{p_2}{p_1}+(\gamma-1)\right]}}\right]^{-2\gamma/(\gamma-1)}, \qquad (4)$$

where p_1 is the atmospheric pressure, p_2 the pressure at the shock tube exit, p_3 the pressure in the driver section, and γ the heat capacity ratio (Schreier 1982; Terao 2007; Needham 2010). The heat capacity ratio, γ, for air is 1.4. The calculated pressure in the driver section for each prescribed pressure at the shock tube exit is listed in Table 4.

Table 4   Pressure in the shock tube

Pressure at the Shock Tube Exit (psig)	Pressure at the Shock Tube Exit (bar) (abs)	Pressure in the Driver Section[a] (bar) (abs)
37.7	3.61	17.98
49.8	4.45	31.79
74.0	6.12	83.81

[a]Estimated

The simulated pressure trace at the pressure transducer location (1/4-inch upstream of the tube exit)—for the case with an incident pressure (at the pressure transducers at the end of the shock tube) of 37.7 psig (2.6 bar gauge) in experiment—in comparison with the measured pressure history at the same location is shown in Fig. 2, along with the pressure traces at other locations (to be described afterward). No test object is present in the test section in this shock tube simulation.
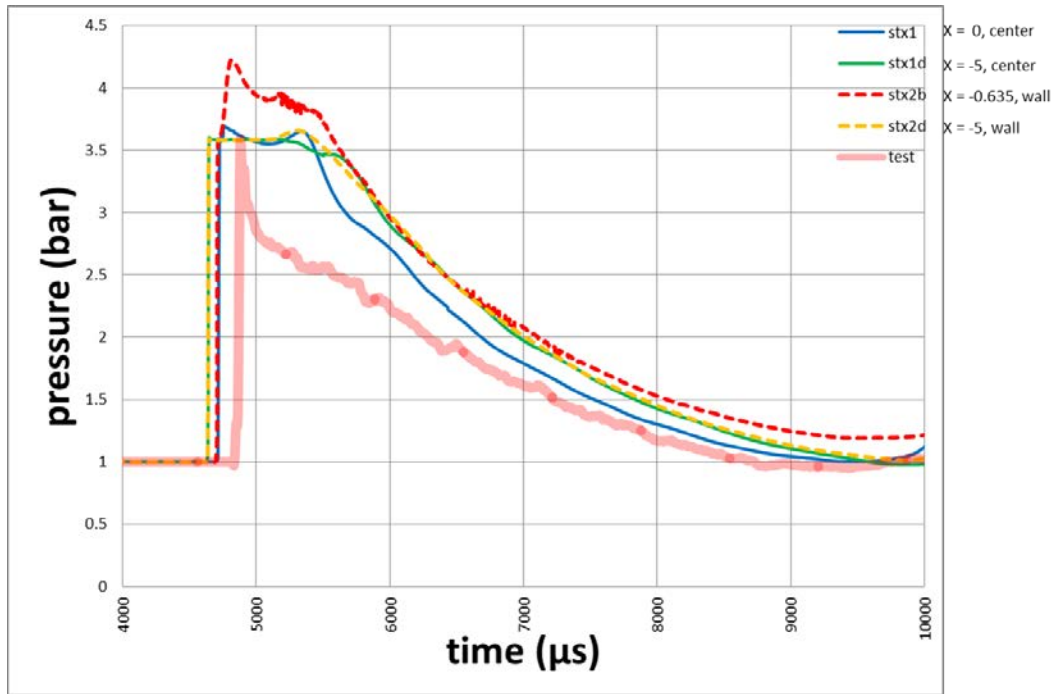
Fig. 2   Comparison of pressure history traces at different tracer locations in simulation. The line marked test is the measured pressure data from the experiment. The locations of the tracers are shown in Fig. 3.

The tracer stx1 is located at the center on the exit YZ-plane (at X = 0). The tracer stx1d is located at the center on the YZ-plane 5 cm upstream from exit (X = –5 cm). The tracer stx2b is located next to the tube wall at 1/4–inch from the tube exit (X = –0.635 cm; i.e., same location as the transducers in experiments). The tracer stx2d is located next to the tube wall at 5 cm upstream from the tube exit (X = –5 cm).

During simulation, the frictionless slip condition is applied on the tube wall in place of an actual frictional turbulent boundary layer. The nodes on the wall are allowed

to slide along the wall surface direction except the last circumferential nodes on the YZ-plane (at X = 0) at the tube exit. However, in this computational scheme, the pressure calculated around these last nodes develops a higher percentage of error, which has been hard to correct. If, instead, we move 5 cm upstream from the tube exit (the YZ plane at X = –5 cm), the calculated pressure shows a more planar 1-D profile (i.e., the pressure at the center of the YZ-plane [tracer stx1d] is practically the same as the pressure near the tube wall on the same YZ-plane [tracer stx2d]). Therefore, the pressure at these locations (stx1d or stx2d) is used for comparison with the measured pressure data from the experimentalists.

The peak pressure in the simulation reaches 3.6×10^{-6} Mbar (2.6 bar gauge or over-pressure)—same as in the experiments. The simulated pressure history still resembles a Friedlander-style pressure profile for a typical explosion in the open but without the negative pressure phase. The pressure unloading being slower in the simulation than in the experiment is probably due to the difference in the rarefaction waves, which appears to be slower in simulation than that in the experiments. The apparent unloading rate may also be affected by the location of the tracer. Moreover, while in simulations the pressure wave running down the shock tube starts out as a planar wave, in experiments the pressure wave jets out the driver section through a small ruptured hole through the center of the Mylar diaphragm such that the pressure wave starts out as a gas jet instead of an idealized planar wave. This gas jet has a higher pressure around the centerline, which will affect the pressure profile further down the shock tube. The ruptured hole also changes the dynamics of the rarefaction wave; it may cause the rarefaction wave to propagate a little faster (than the planar wave in simulation). But how far the rarefaction wave has run over the shock wave front is not knowable from the experimental data. For further details, see the Appendix, which includes discussion about the effect of mesh resolution.

4.2 Comparison with Measured Porcine Head Surface Pressure

The porcine test object is placed next to the exit of the shock tube, with its right side facing the exit of the shock tube (Fig. 3).
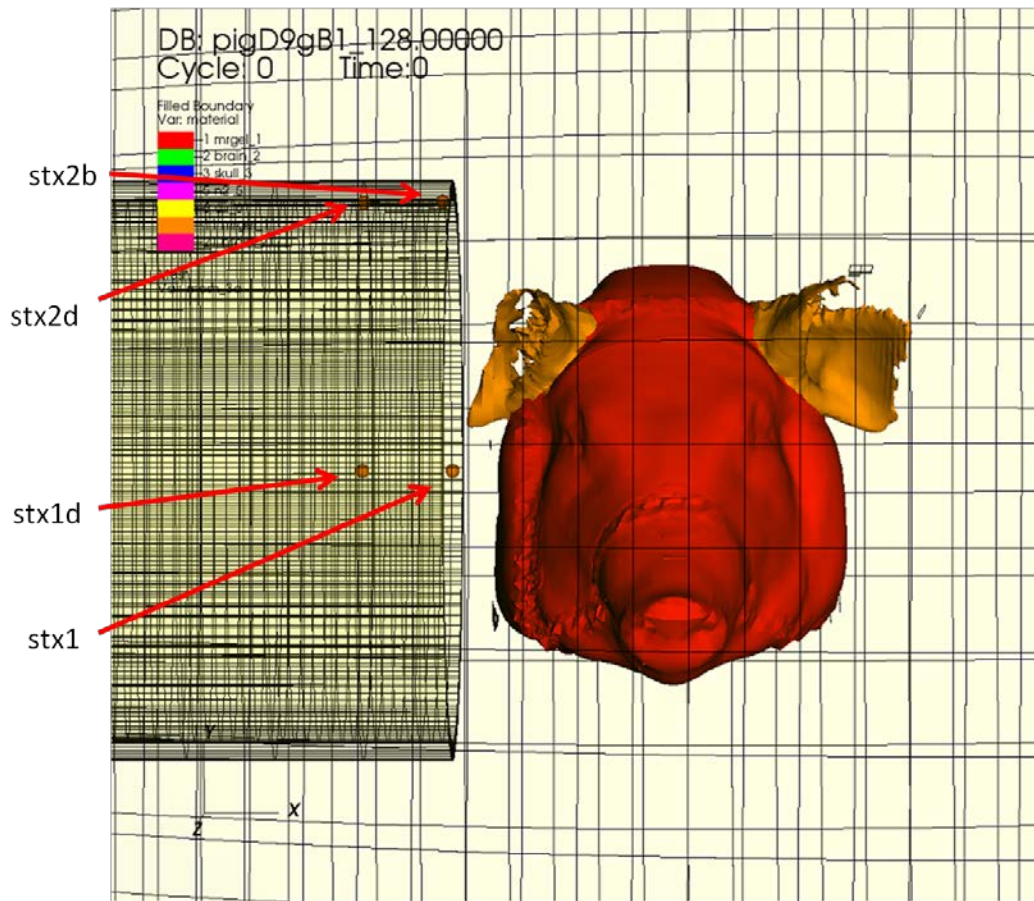
Fig. 3   Porcine head outside the exit of the shock tube

Figure 4 shows the tracers mentioned in the various sections on the Z = –2 plane. However, the pressure transducers and the accelerometer may not be on the same plane in the experiment.
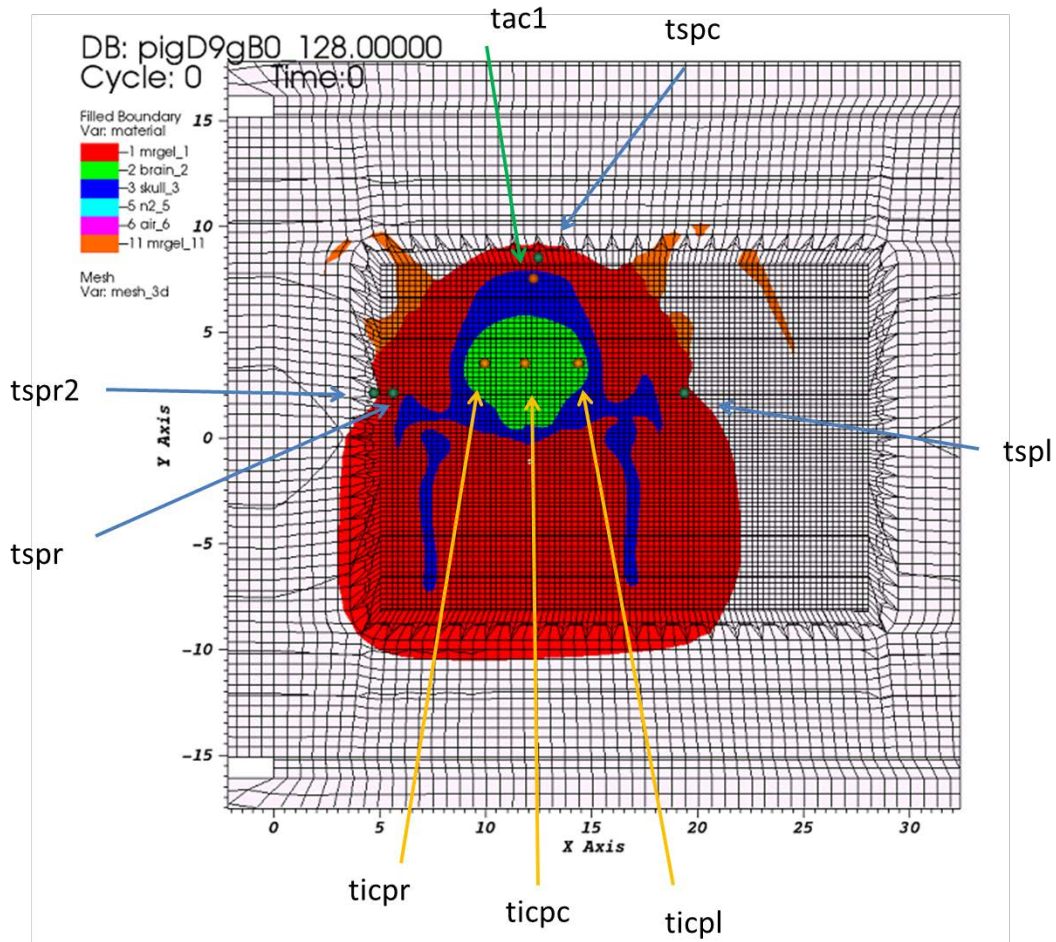
Fig. 4   Locations of tracers mentioned in the various sections (Z = –2 plane)

Figure 5 shows the locations of the tracers in the coarser mesh.
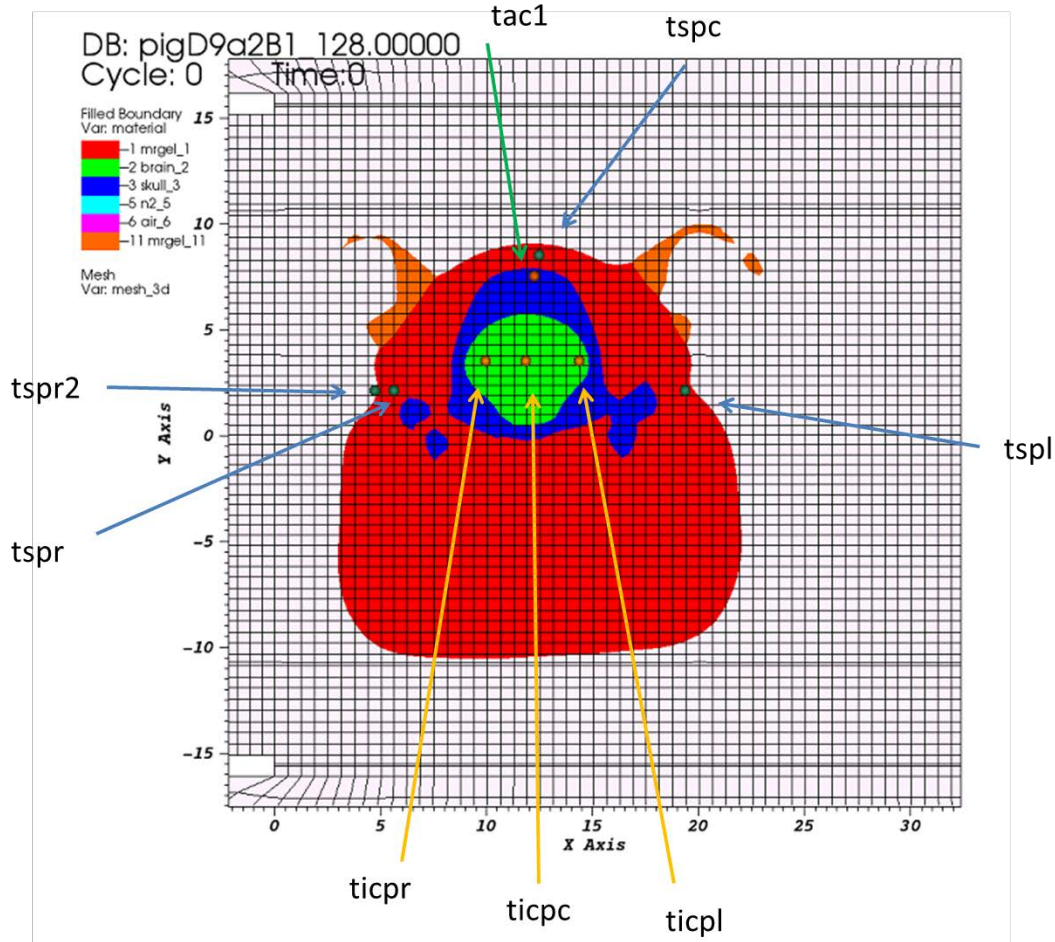
Fig. 5   Locations of the tracers in the coarser mesh (Z = –2 plane)

Pressure sensors are placed on the right, top, and left side of the porcine head for the surface pressure measurements. Figure 6 shows the simulated surface pressure (fine mesh) compared with the measured surface pressure for tests with an incident blast pressure of 37.7 psig (2.6 bar gauge) (C Bass; personal communication; November 2010; unreferenced). The pressure in the simulation on the right side of the porcine face follows the Lagrangian tracer, tspr, initially in a nonmixed host element beneath the skin. The host element may become a mixed element with which the tracer drifts along due to head movement during impact. To improve comparison, another tracer tspr2, a Eulerian tracer, is added just outside the skin surface. The pressure history at this Eulerian tracer location initially follows the experimental measurement closely; however, the relative distance of this tracer point to the surface of the porcine face increases with time because the porcine head moves with the blast. The pressure at tspr stays higher a little longer than in experiment. This may relate to the flat top in simulation instead of a sharp top in

experiment (Fig. 2). In the figure, tspc (Lagrangian tracer) is the pressure history at a center top location on the skin surface, and tspl (Lagrangian tracer) is the pressure history at a location on the left side of the skin surface.

At the moment of blast impact, the peak pressure reaches around 7 bar. When the over-pressure reaches 15 psi (1.034 bar, 103.4 kPa gauge), there is a 50% chance of eardrum rupture in a human (Owen-Smith 1979).
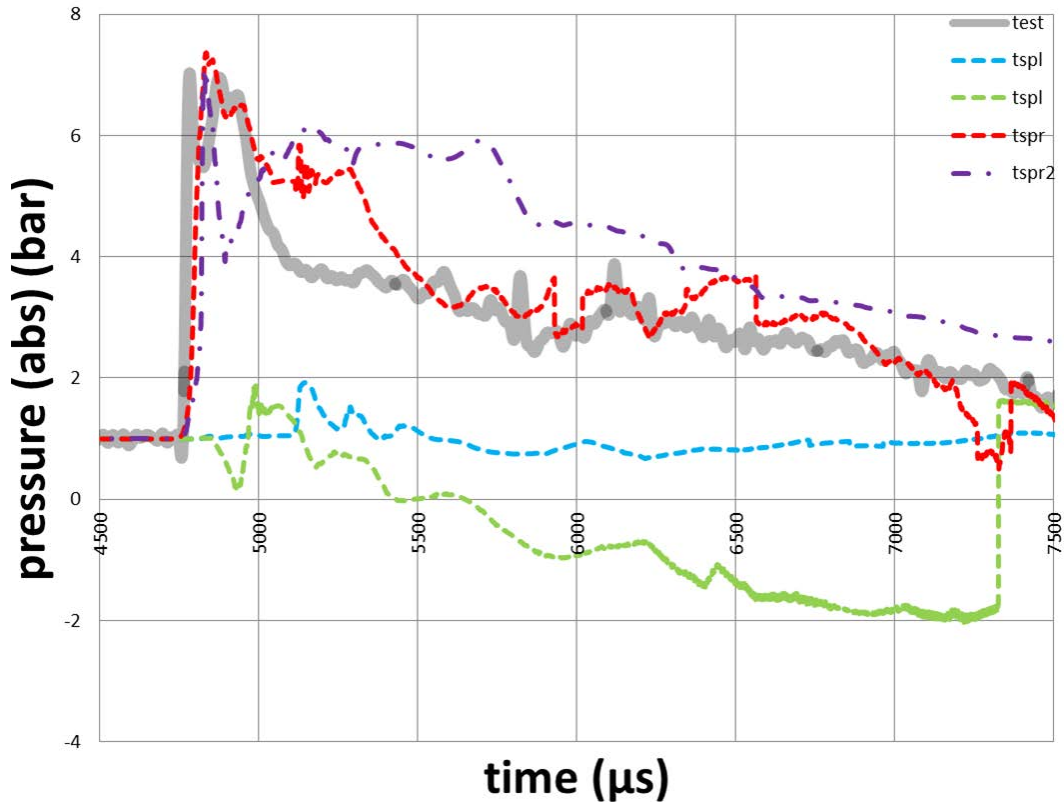
Fig. 6   Simulated surface pressures (fine mesh) compared with the measured surface pressure (right face)

4.3   Comparison with Measured Intracranial Pressure

There are 3 Lagrangian tracer points within the brain (Fig. 4) for the intracranial pressure measurements: one right, one near the top, and one left. Figure 7 shows the intracranial pressures at these tracer locations for the test with an incident pressure of 49.8 psig (3.44 bar gauge).
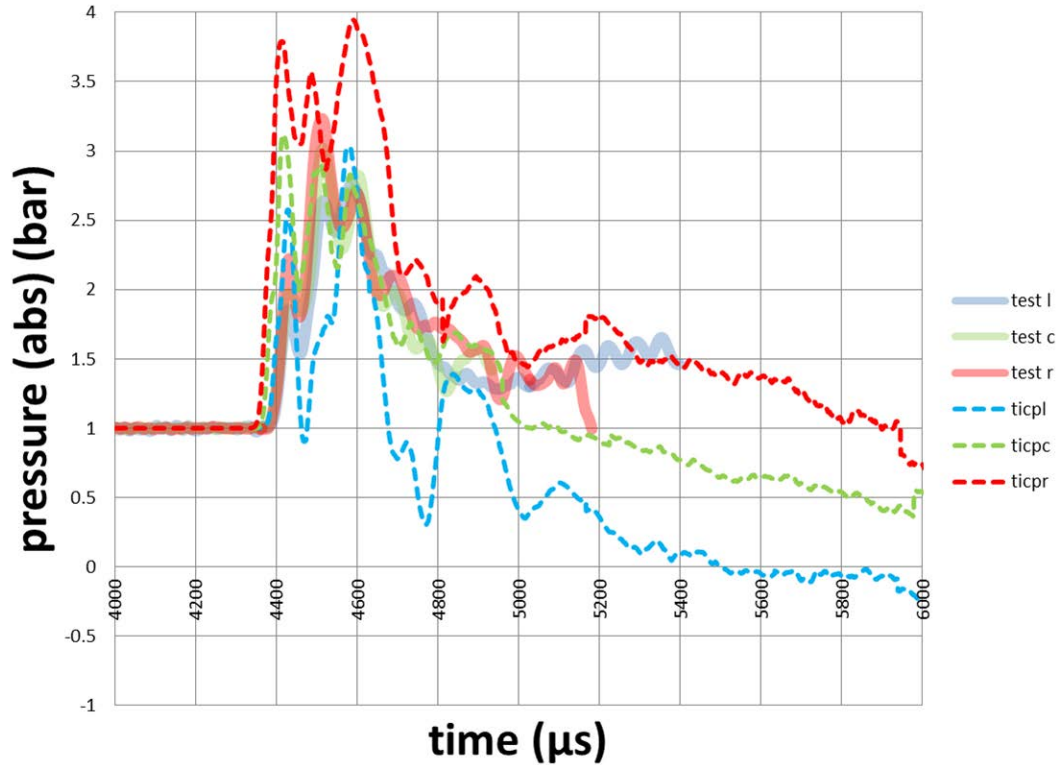
Fig. 7   History of the intracranial pressures (fine mesh) compared with the measured pressures during tests. However, the piezo-resistive pressure transducers will not be able to pick up negative (abs) pressure values.

The plot is separated out into 3 plots: one for right, one for center, and one for left each; along with the lower and upper bound lines from each test data set and the simulation result using the coarser mesh. Figure 8 shows such a plot for the intracranial pressure on the right side (tracer ticpr, facing the shock tube).
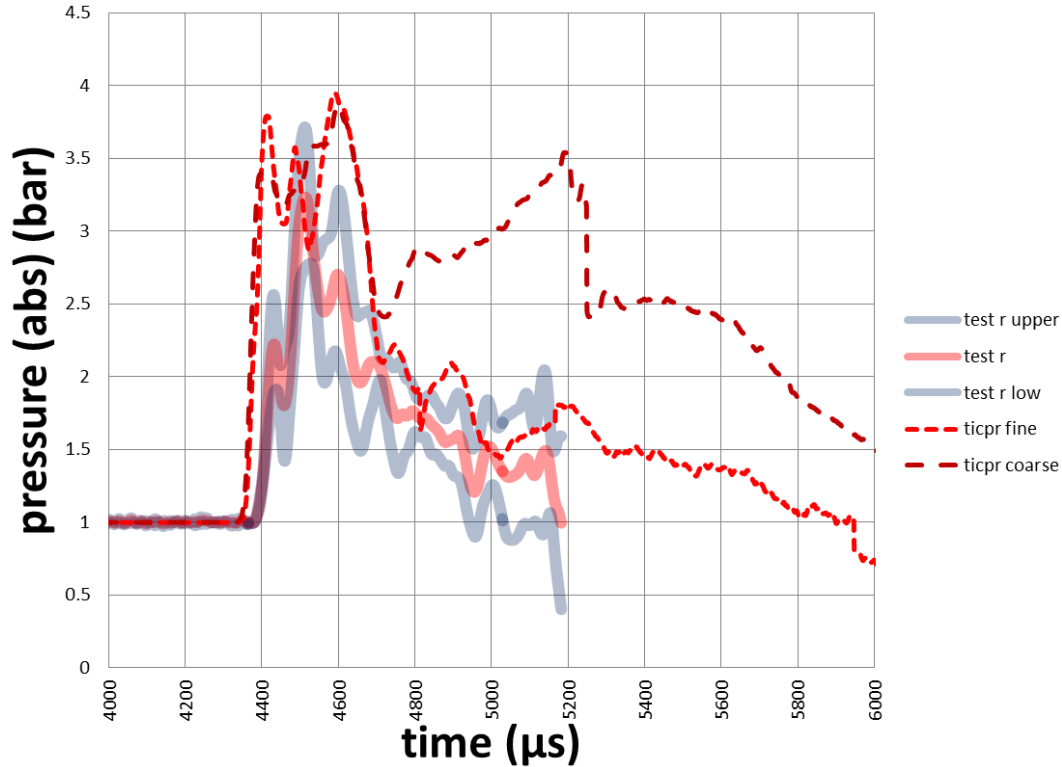
Fig. 8   Intracranial pressure on the right side. Test data are shown with their lower and upper bounds. The pressure in simulations show the results from the finer mesh and from the coarser mesh.

The intracranial pressure on the right side (tracer ticpr) peaks around 3.7 bar, similar to the measured data in the first ms after the blast impact. The simulated pressure with finer mesh (ticpr) is not far off the test data. The simulated pressure with the coarser mesh is initially similar to the result with the finer mesh. The sudden jump in pressure shown in the coarse mesh (Figs. 8–10) may come from the effect of tracer drift and the effect of the mixed elements. Other differences between the simulated pressure and the test data may come from factors such as the location of the tracer, the geometry differences between the digital model and the real test object, and difference in pressure loading.

Figure 9 shows the plot for the intracranial pressure at the center location (tracer ticpc).
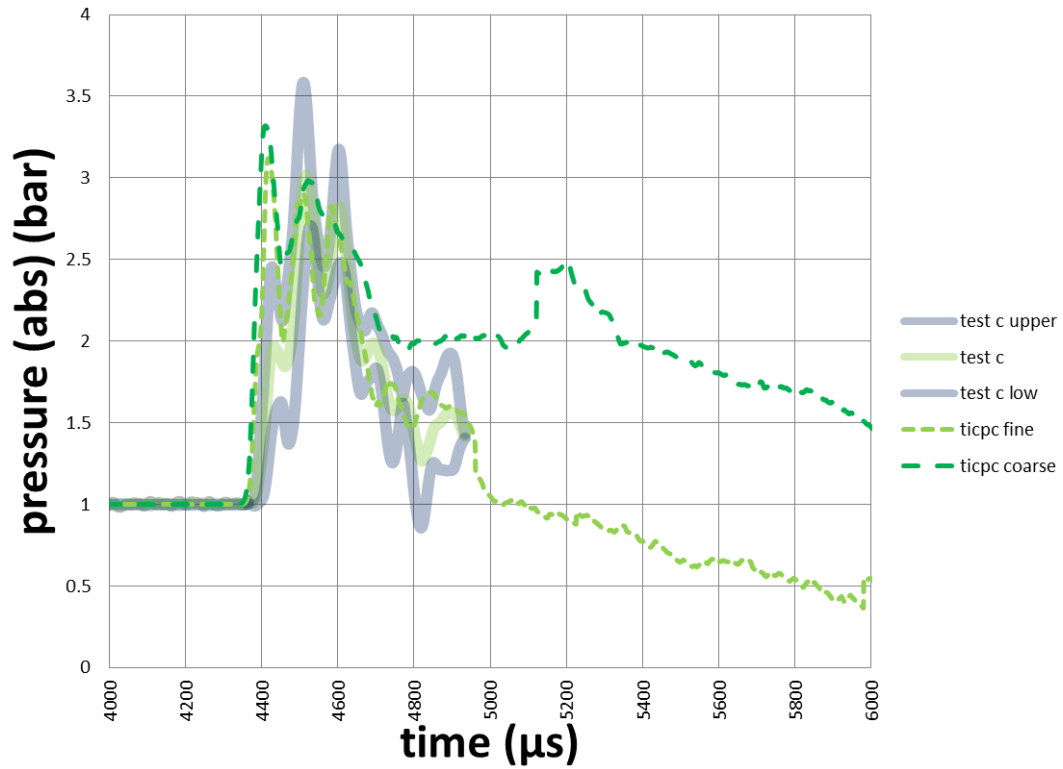
Fig. 9 **Intracranial pressure at the center location. The test data are shown with their lower and upper bounds. The pressure in simulations show the results from the finer mesh and from the coarser mesh.**

Figure 10 shows the plot for the intracranial pressure on the left side (tracer ticpl).
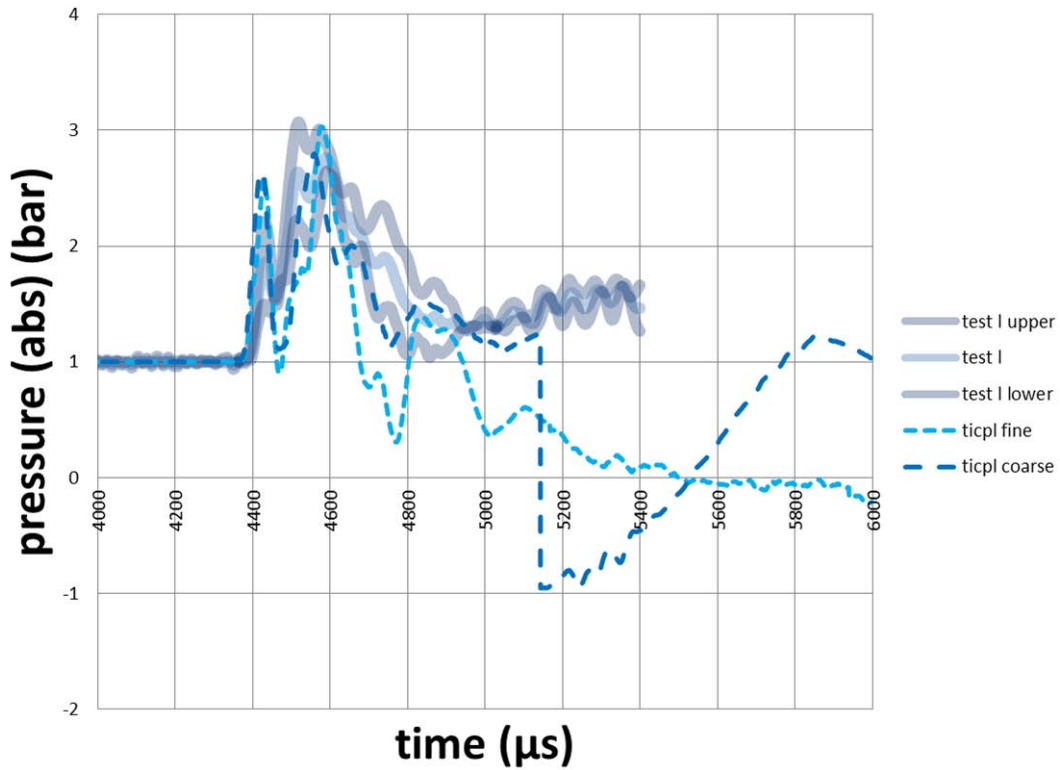
Fig. 10 Intracranial pressure on the left side. The test data are shown with their lower and upper bounds. The pressure in simulations show the results from the finer mesh and from the coarser mesh.

The tracer points drift with the head, which moves with time. Figure 11 shows the history of the X coordinates of the tracer points (fine mesh).

At the moment of impact, the intracranial pressure reaches above 3 bar. Intracranial pressure exceeding 34 psi (gauge) (2.3 bar) has been linked to high probability of severe injury for human brains (Ward 1978; Ward and Chan 1980).
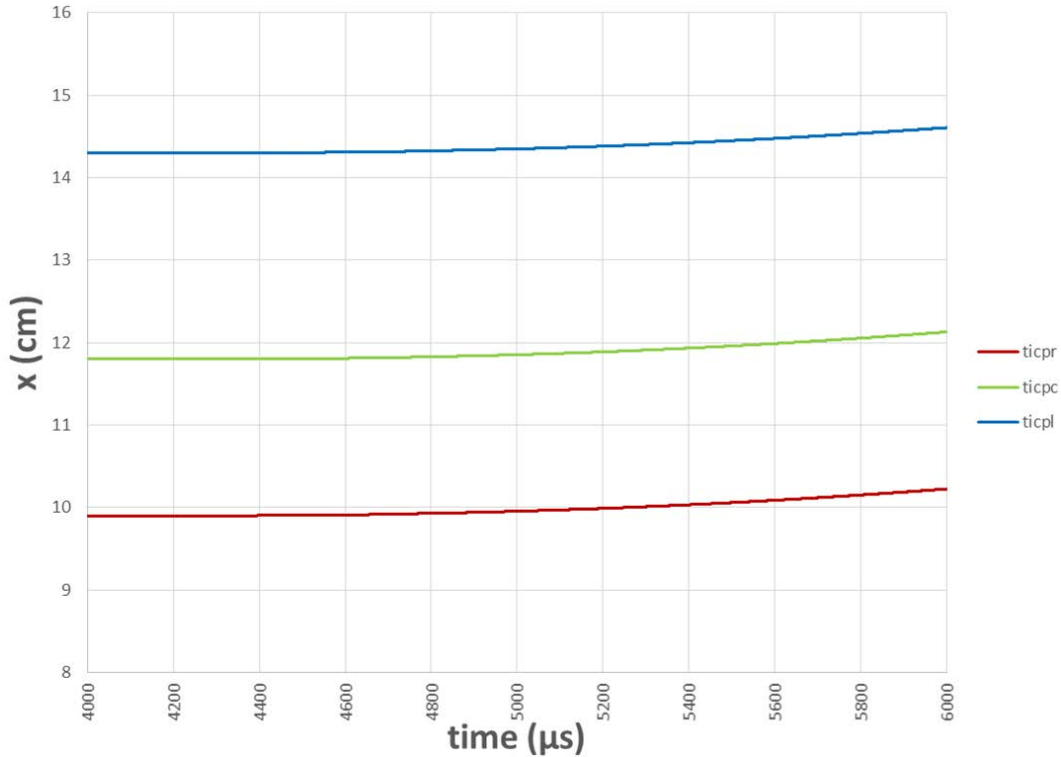
Fig. 11 **History of the X coordinates of the tracer points: ticpr, ticpc, and ticpl (fine mesh)**

4.4 Comparison with Measured Acceleration Data

An accelerometer box is attached to the top of the skull for measuring the acceleration of the porcine head during the tests. Figure 12 shows the acceleration in simulation compared with measured data for the test with an incident pressure of 37.7 psig (2.6 bar gauge). The Lagrangian tracer location tac1 is located near the top of the skull, similar to the location of the accelerometer box during the tests; the Lagrangian tracer ticpc is located within the brain, which does not have a corresponding test data set. The tracer sampling rate is 1 μs, same as in experiment. The amplitude of the acceleration at tracer tac1 (~612 g)—being lower than the measured data (~1,000 g)—may come from a combination of factors, e.g., the difference in mass between the digitized head and the real head, the transient data surge of the instrumentation, and/or the smoothing or averaging effect in time and space. Lowering the density of skull can increase the acceleration, but it will also increase the sound velocity in the skull. The amplitude of acceleration at tracer ticpc (brain) is slightly higher while using the finer mesh (~400 g) than using the coarser mesh (~360 g).

17
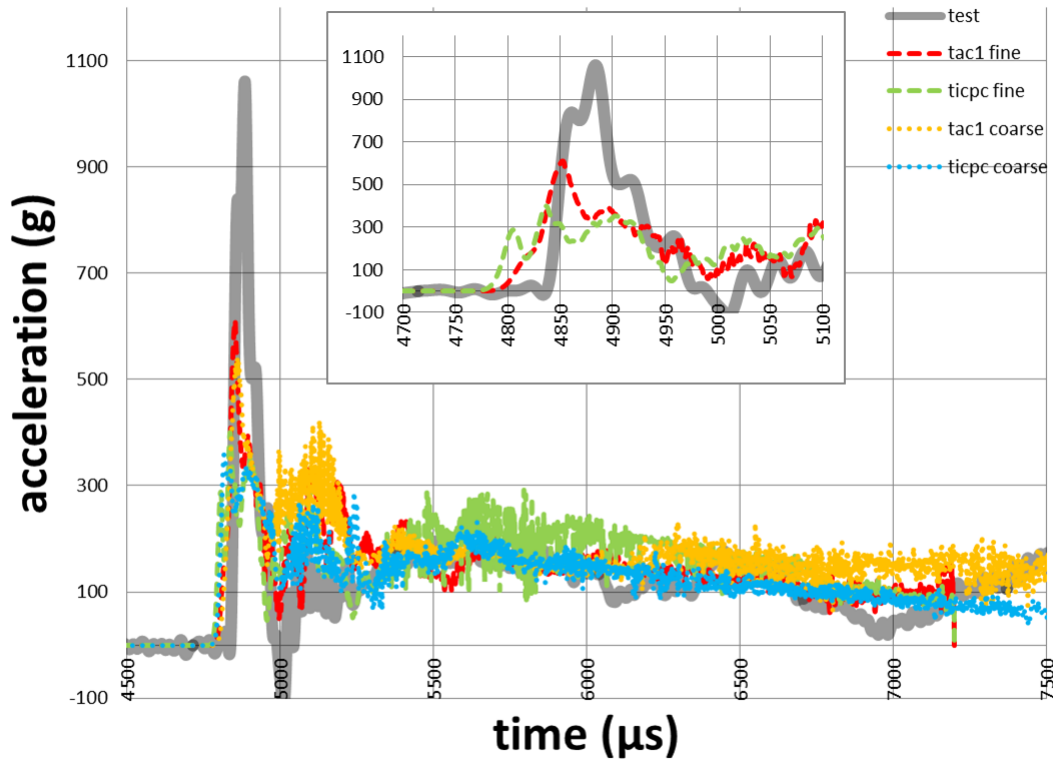
Fig. 12   Cranial acceleration history. Inset shows the close-up around the spike. The tracer tac1 corresponds to the location of the accelerometer in the tests. The tracer ticpc is inside the brain and has no corresponding experimental measurement data.

The negative phase in the measured acceleration suggested that the accelerometer may have sprung back during the initial impact. The measured acceleration history shows a superposed higher frequency oscillation with a wave length around 35 μs. It may come from pressure waves in the head, which travel about 5 cm in the brain in 35 μs and about 6 cm in the skull in 35 μs.

Figure 13 shows the accelerations at the tracer tac1 (accelerometer location) both from simulations with the finer mesh and with the coarser finite element mesh.
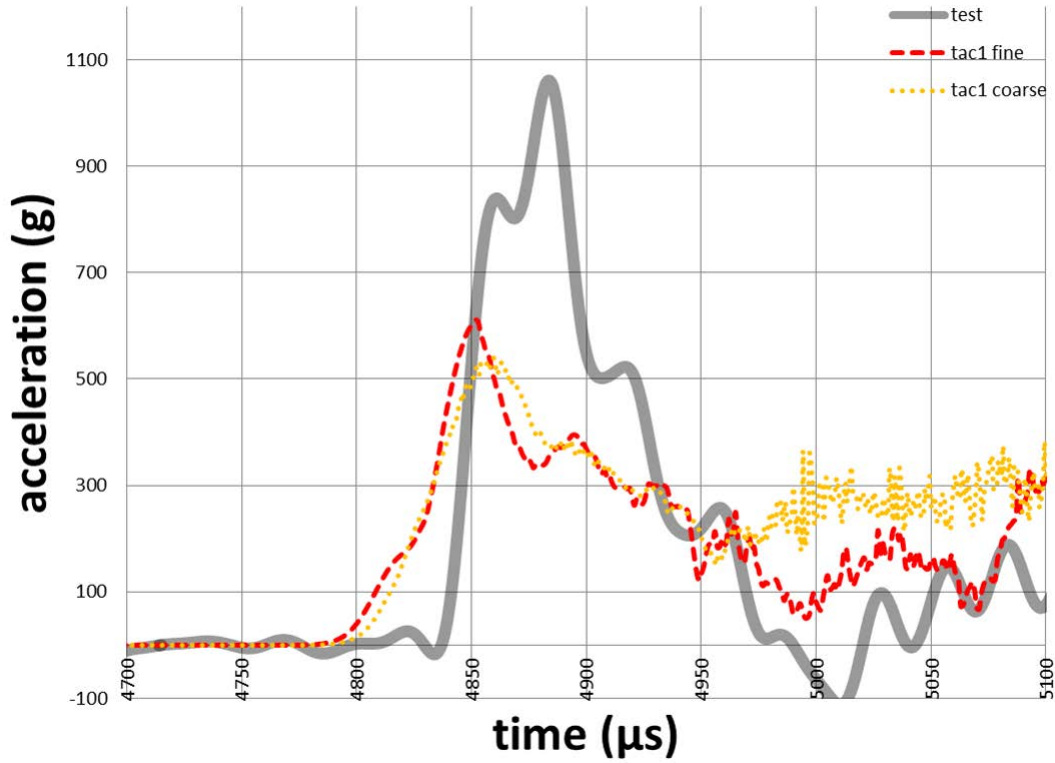
Fig. 13   Cranial acceleration history. The tracer tac1 corresponds to the location of the accelerometer in the experiments.

Figure 14 shows the accelerations at the tracer ticpc (within the brain) both from simulations with the finer mesh and with the coarser mesh.
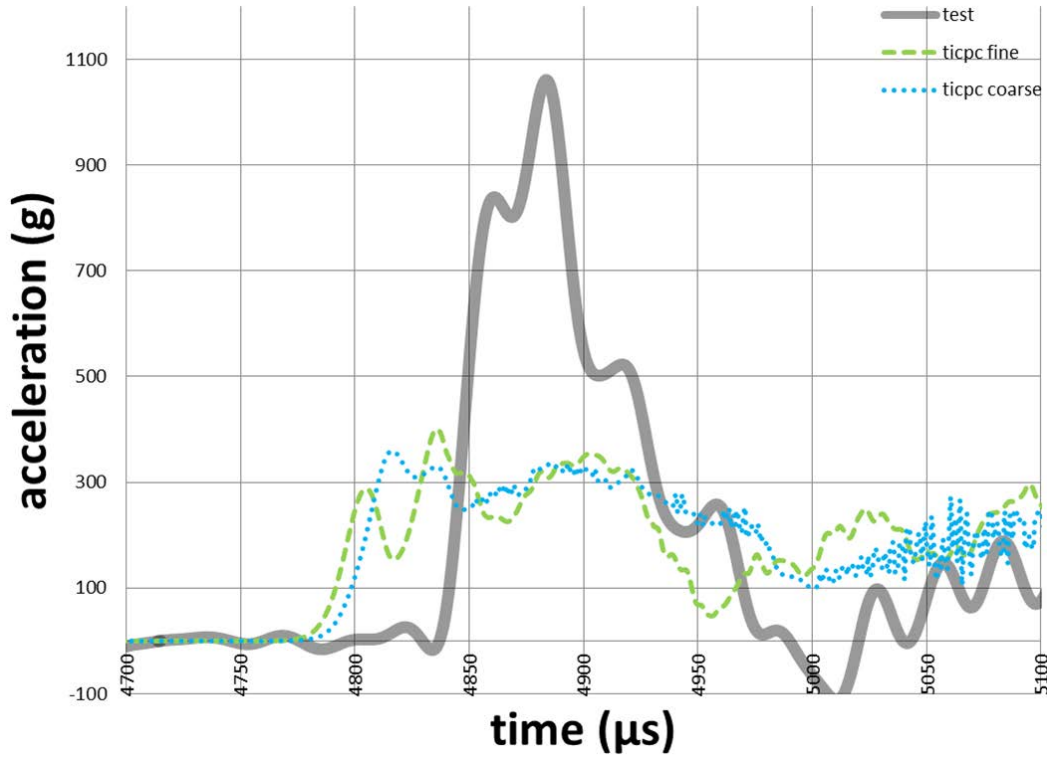
Fig. 14 **Cranial acceleration history. The tracer ticpc is inside the brain and has no corresponding experimental measurement data (the line marked test is the same as previous—at the accelerometer location).**

5. Additional Calculated Variables

5.1 The Coup and Contrecoup Profile

The blast wave of the shock tube impacts on the right side of the porcine head. The intracranial pressure on the right side of the porcine head reaches above 3 bar (abs) at around 4,500 µs (Fig. 15).
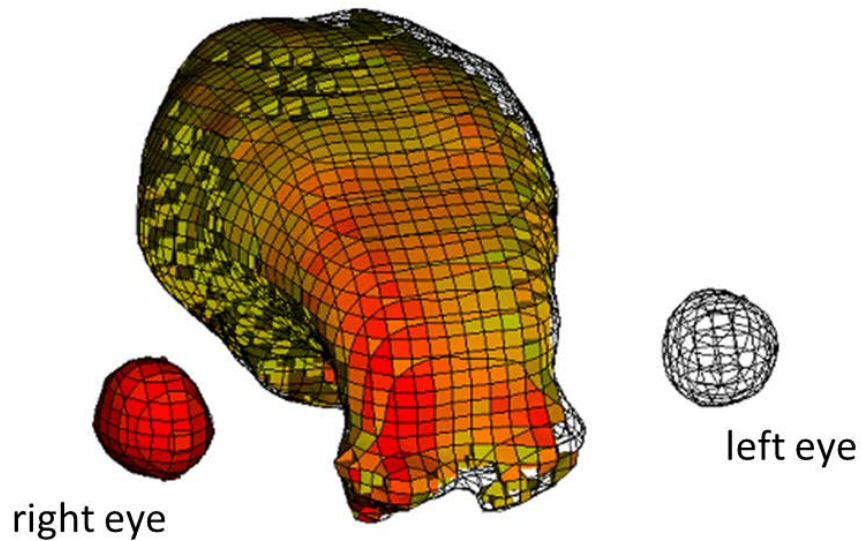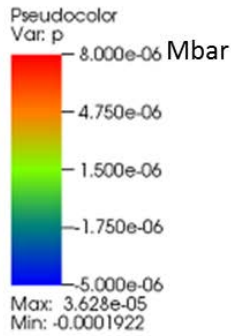
Fig. 15　Regions in color at 4,500 μs have pressure above 3 bar (abs). Finite element mesh shows the brain and eyes of the pig.

The pressure wave then traverses to the other side of the brain along the impact direction. At 5,000 μs, negative pressure builds up on the other side (nonimpact side) of the brain (Fig. 16). The subsequent pressure wave on the opposite side from the initial impact (coup) is called the contrecoup in the literature.

21
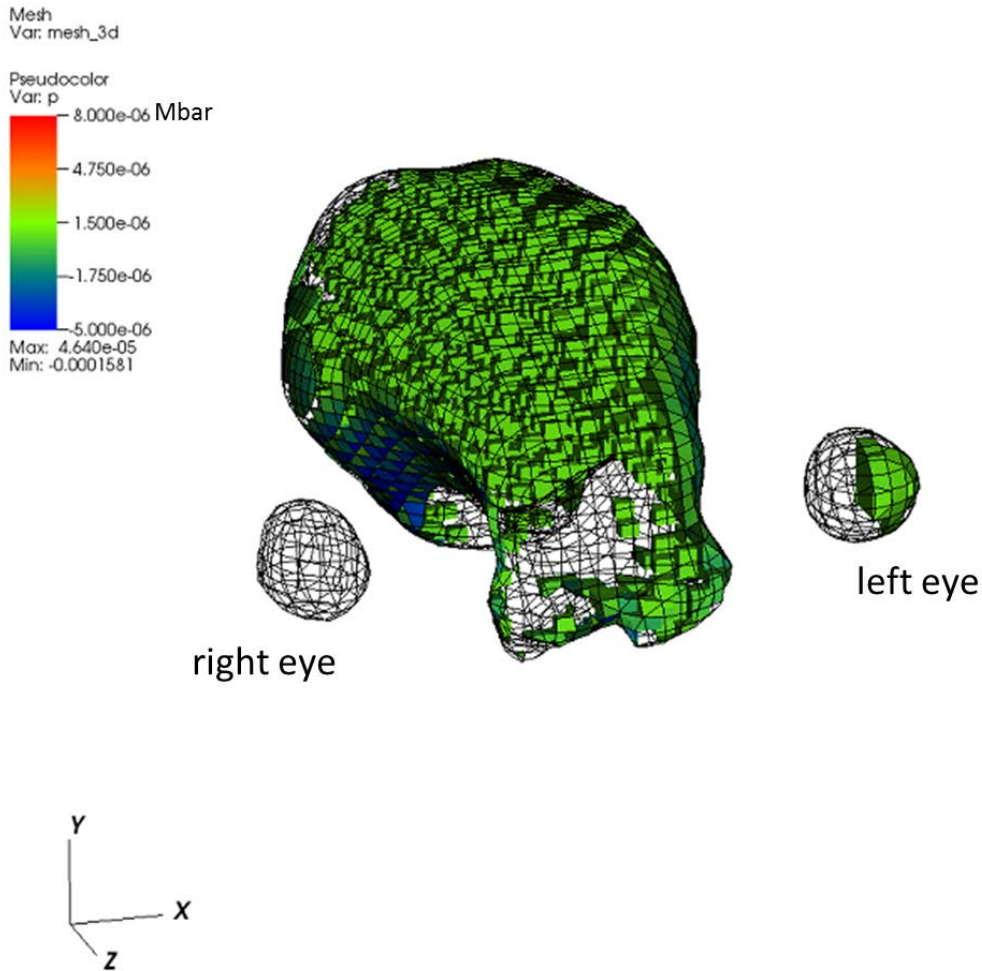
Fig. 16   Regions in color at 5,000 μs have pressure (abs) below 1 bar (~1 atm)

When the pressure falls below certain critical level, cavitation may occur. The critical vaporization pressure changes with temperature. At normal porcine body temperature (about 39 °C) the water vaporization pressure is about 7 kPa (0.07 bar) (Malley 2005; Herbert et al. 2006). The vapor pressure of blood is equivalent to a saline with 0.9 g of sodium chloride per 100 g of water (Culbert 1935). Its vapor pressure will be a little lower (less than 1-mm Hg [≈133 Pa]) than that of water (Kientzler et al. 1952). Since 99% of the cerebrospinal fluid (CSF) is water, its vapor pressure is likely similar. If cavitation does occur in the vasculature (blood) or in the CSF, it generates tiny gas bubbles that may negatively impact the normal function of the brain; too many gas bubbles can be detrimental or even lethal (Brennen 1995; Brennen 2006). The process of cavitation can further change the subsequent pressure field in the surrounding region of the brain. Figure 17 shows the profile of pressure regions below 0.07 bar.
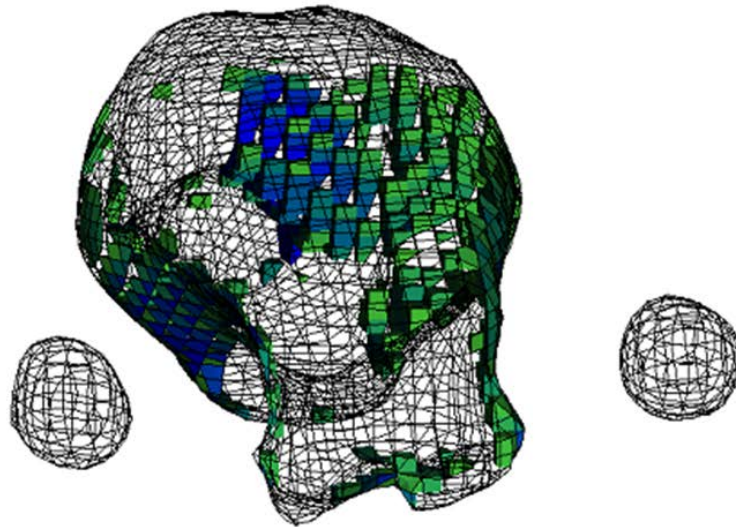
Fig. 17 **Regions in color at 5,000 μs have pressure below 0.07 bar (abs), where the cavitation may ensue**

Adding information about the vasculature orientations into mesh will enhance the accuracy of simulation (Omori et al. 2000; Ho and Kleiven 2007). With the vasculature orientation in the mesh, the stress along the vasculature or the shear across the vasculature can be calculated more accurately.

5.2 The Deformation of the Skull

McElhaney (1976) discussed the mean strain criterion (MSC) as an indicator of head injury, where mean strain is defined as the displacement of one side of the head relative to the other, divided by the distance across the cranium. Impact tests with various sized primates to produce minor, but identifiable brain injury show that the MSL of 0.0329 inches/inch is tolerable for Rhesus monkeys subjected to rigid striker impacts. A tolerable mean strain level of 0.0061 inches/inch has been predicted by the MSC model for fresh intact cadaver (McElhaney 1976). Furthermore, the maximum tolerable skull deformation has been estimated to be approximately 0.02 inch (Fan 1971). Since the impact surface area of a blast is larger than that of a focused impact, these estimates from tests with focused impacts could be used as a guide but need modification to find the tolerable stain level for the blast impact.

Figure 18 shows the relative strain from 2 tracers at opposite sides of the cranium for the case of an incident pressure of 2.6 bar (gauge).
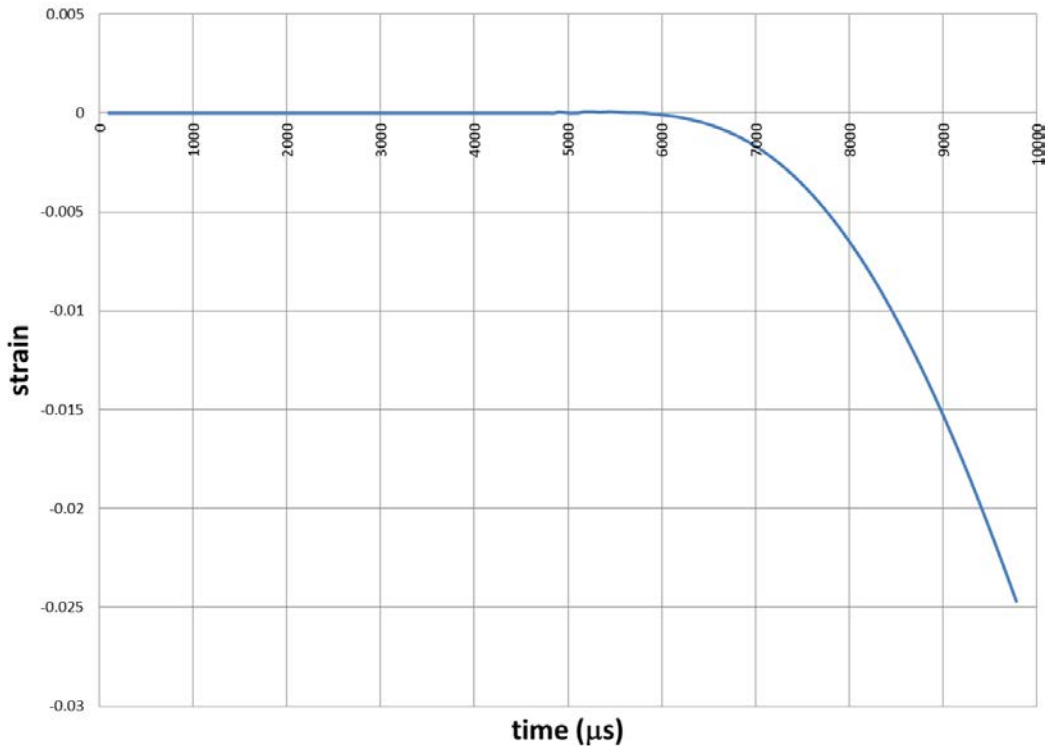
Fig. 18   Mean strain across the cranium

The head injury appears to be probable for the simulated porcine head; however, the elastic model for the skull may have overestimated the magnitude of the strain (Powell et al. 2012).

5.3 Strain in the Brain

Figure 19 shows the equivalent strain profile at 9,800 µs at about 5 ms after blast. It has been estimated that with a strain greater than 20%, the axotomy (axonal disconnection) will result from membrane fragmentation and cytoskeletal proteolysis (Maxwell 1997).

Another cumulative strain damage measure, based on the calculated volume fraction of the brain that has experienced a specific level of stretch, has been used as a predictor for deformation-related brain injury. The measure is based on the maximum principal strain calculated from a strain tensor obtained by integration of the rate of deformation tensor (Bandak and Eppinger 1994).

Adding information about the nerve fiber orientation into mesh will enhance the accuracy of simulation (Chatelin et al. 2011; Wright and Ramesh 2012; Dagro et al. 2013). With the nerve fiber orientation in the mesh, the stress along the nerve fiber or the shear across the nerve fiber can be calculated more accurately.
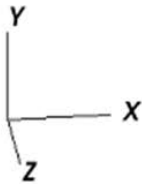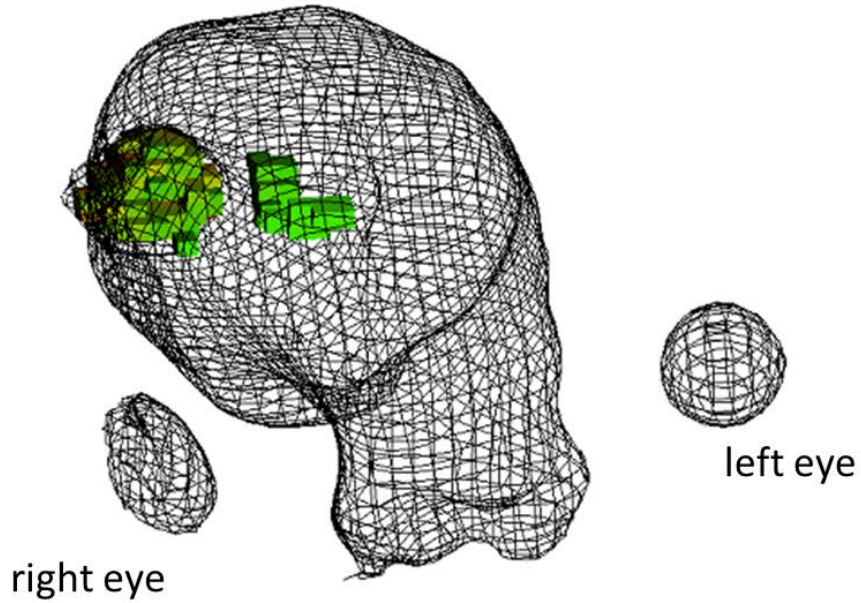
Fig. 19   Regions in color at 9,800 μs have equivalent strain greater than 0.15

5.4 The Effective Stress (von Mises Stress)

Figure 20 shows the profile of the effective stress (or von Mises stress) at 9,800 μs at about 5 ms after blast. The effective stress ranges from 0 to 0.13 bar (13 kPa) in the brain. The von Mises stress is defined as

$$\bar{\sigma}_e = \sqrt{\frac{3}{2}\sigma'_{ij}\sigma'_{ij}} \; . \tag{5}$$

26

On the (σ_1, σ_2) stress space, the maximum shear (Tresca yield surface) is within the envelope of von Mises stress. Shear stress in the midbrain of the brainstem at 7.8 kPa level has been correlated with 50% probability of mild traumatic brain injury (mTBI) (Zhang et al. 2004).
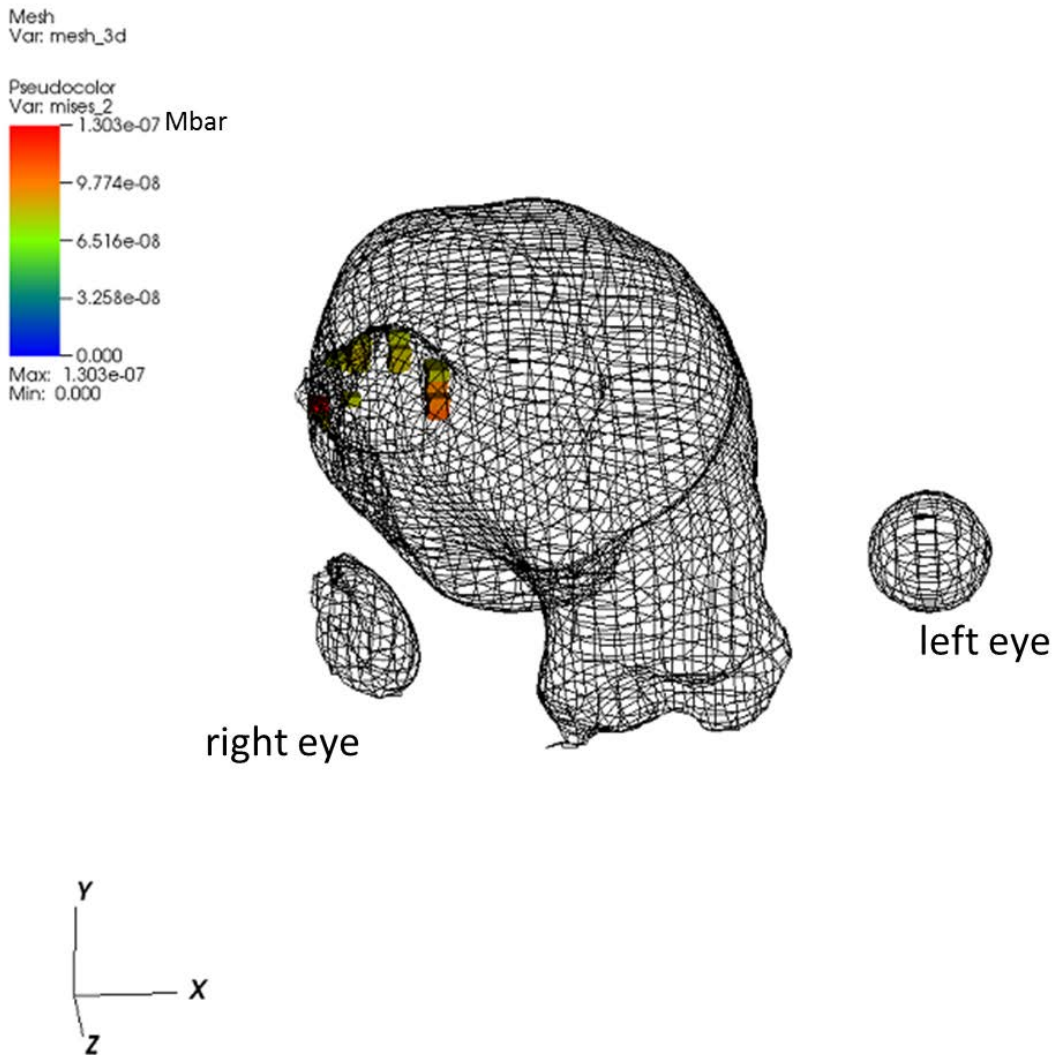
Fig. 20   Regions in color at 9,800 µs have von Mises stress greater than 7.8e-2 bar (7.8 kPa)

5.5 Deviatoric Strain Energy

Figure 21 shows the profile of the deviatoric strain energy at 9,800 µs at about 5 ms after blast. Higher deviatoric strain energy may lead to regional injury.

27
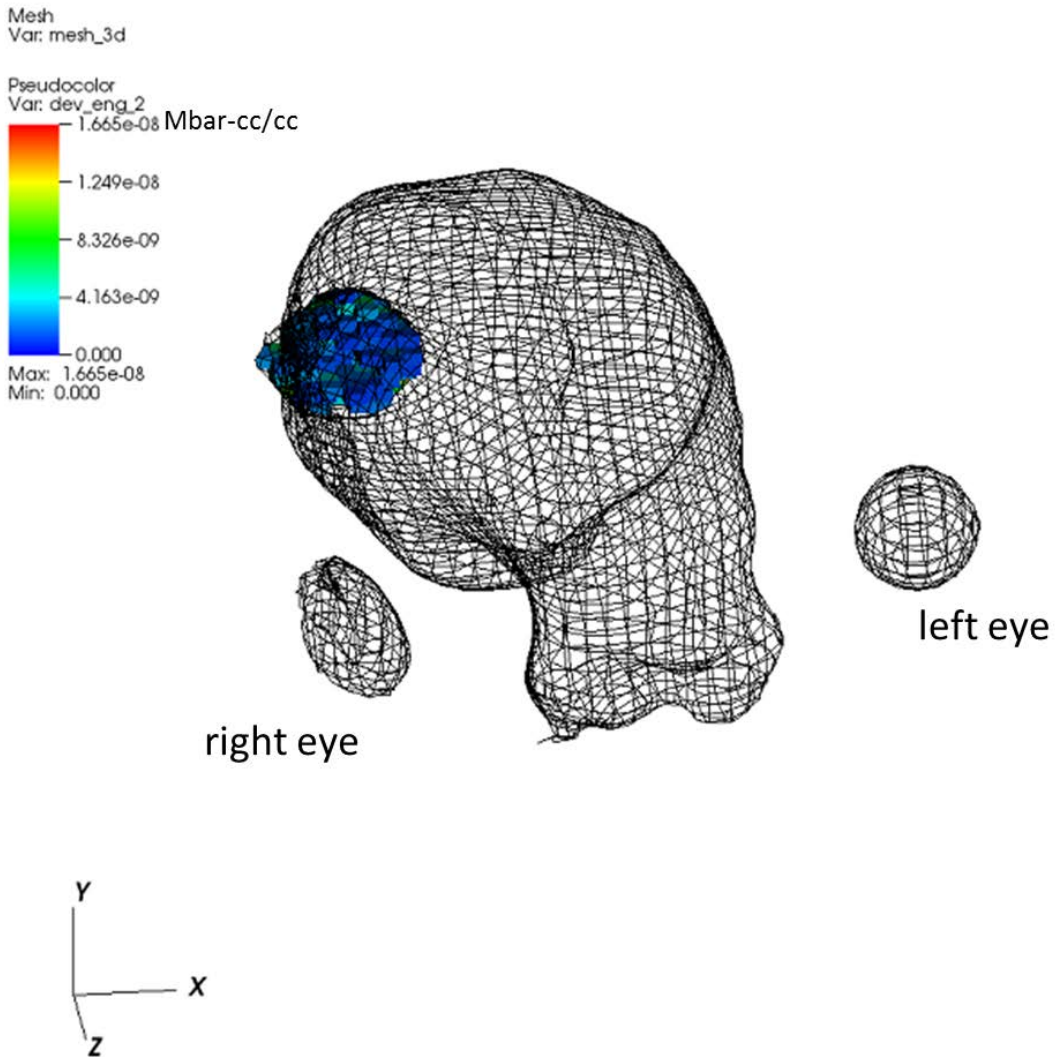
Fig. 21   Regions in color at 9,800 μs have deviatoric strain energy greater than 1.e-3 bar-cc/cc (1.e-4 J/cm^3) (threshold not established yet)

5.6 Löwenhielm Vein Injury Criterion

Stress tests with parasagittal bridging veins from the lateral convexity of the brain show that the vein's strain capacity is dependent on strain rate; maximal strain is markedly reduced as the rate was increased (Löwenhielm 1974; Takhounts 2003). The border line in the strain rate and strain space can be fitted to the relationship

$$\varepsilon_{critical} = 0.0608 \, (\log_{10}(\dot{\varepsilon}))^2 - 0.4414 \, (\log_{10}(\dot{\varepsilon})) + 0.9872 \, , \qquad (6)$$

where $\dot{\varepsilon}$ is strain rate in 1/s.

Figure 22 shows the profile of $\left(\dfrac{\varepsilon}{\varepsilon_{critical}}\right)$, where the equivalent strain and equivalent strain rate are used in place of strain and strain rate. Higher $\left(\dfrac{\varepsilon}{\varepsilon_{critical}}\right)$ ratio shows a higher possibility of vein injury. When $\left(\dfrac{\varepsilon}{\varepsilon_{critical}}\right)$ is greater than 1, the strain will be large enough to show vein injury. In Fig. 22, the regions in color have $\left(\dfrac{\varepsilon}{\varepsilon_{critical}}\right)$ greater than 0.015.
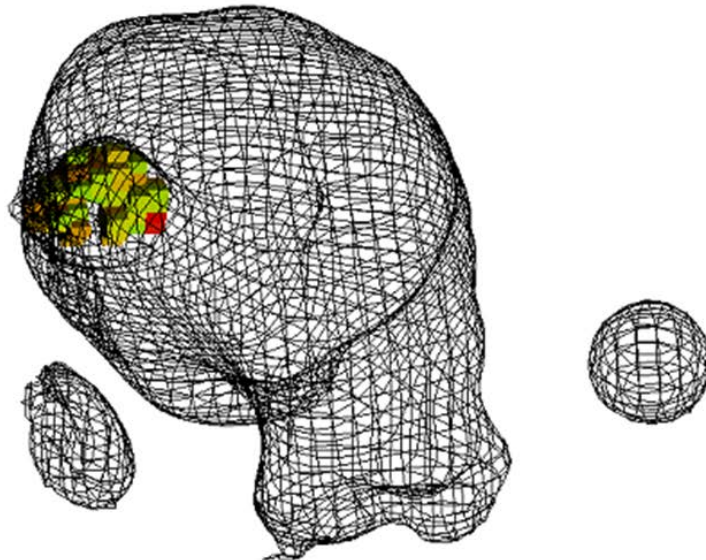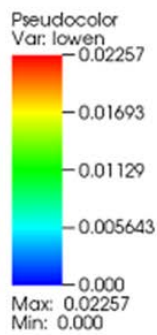
Fig. 22   Regions in color at 9,800 μs have $\left(\dfrac{\varepsilon}{\varepsilon_{critical}}\right)$ greater than 0.015. It may increase with time

5.7 Viscous Injury Criterion

Rapid motion of the skull causes displacement of the skull against the soft tissues of the brain, which lag in their motion due to inertia and loose coupling to the skull. Relative displacement between brain and skull produces deformation of brain tissue and stretching of bridging veins, which contribute to the tissue-level causes of brain injury. The brain compliance approach interprets brain deformation by the viscous response (VC) or the product of strain and strain rate at the tissue level. The viscous response is a measure of the viscoelastic reaction of tissue to dynamic deformation and combines 2 parameters of soft tissue injury: strain (compression, C) and strain rate (velocity of deformation, V). The viscous response is representative of the absorbed energy through kinetic energy conversion (Lau 1986; Viano 1988; Zhang 2003). The estimated threshold for 25% of mild traumatic brain injury is 14/s (or 1.4e-5/μs) (Zhang 2003). Figure 23 shows the profile of the VC or ($\varepsilon \cdot \dot{\varepsilon}$) at 9,800 μs at about 5 ms after blast. The equivalent strain and equivalent strain rate are used in placed of strain and strain rate.

Fig. 23   Regions in color at 9,800 μs have VC or ($\varepsilon \cdot \dot{\varepsilon}$) greater than 1.4e-5/μs

5.8 Linear Accelerations

Test data from frontal hammer blows and air blasts to the exposed brain, drop tests of human cadaver heads (Wayne State Tolerance Curve), and concussive data from animals as well as long-duration human sled experiments have led to the Gadd Severity Index. The injury assessment is based on the average acceleration and pulse duration, since the injury survivability of brain increases if the duration of the pulse decreases. For that, an effective acceleration is defined as $A = \frac{1}{(t_2 - t_1)} \int_{t_1}^{t_2} a(t)dt$, where a(t) is the acceleration and (t_2 – t_1) represents the duration. A head injury criterion (HIC) is defined as HIC =

$\max \left[\frac{1}{(t_2-t_1)} \int_{t_1}^{t_2} a(t)dt\right]^{2.5} (t_2 - t_1)$, which is adopted as the head injury standard for Federal Motor Vehicle Safety Standard 208 (Ewing et al. 1968; Versace 1971; Hess et al. 1980; Ommaya 1981; Kleinberger et al. 1998; Eppinger et al. 1999; King 2000).

For the incident pressure of 37.7 psig (2.6 bar gauge), the calculated HIC for the blast simulation is around 10 (based on $\Delta t = 5$ ms; based on the acceleration at the Langrangian tracer tac1 [the accelerometer location]). Since the blast peak acceleration surge duration is typically only a few tens of microseconds compared with the acceleration duration in a vehicle collision typically of a few tens of milliseconds, the conventional HIC criterion developed for motor vehicle safety is not suitable for the blast impact. A more relevant formula developed specifically for blast impact should take this shorter acceleration duration into consideration.

Another acceleration inspired measure named the skull fracture correlate (SFC) is defined as $SFC = \frac{\Delta V_{HIC}}{\Delta T_{HIC}}$, where ΔV_{HIC} is the change in velocity and ΔT_{HIC} is the HIC time interval. For 15% or less probability of skull fracture, the threshold is SFC < 124 g with a 95% confidence band of 96 < SFC < 144 g. The SFC correlation is established based on logistic regression against an extensive set of post mortem human specimen data (Vander Vorst et al. 2003; Chan et al. 2006). These fracture correlations developed from drop tests could be referenced and modified for finding the corresponding threshold for blast impact.

For the incident pressure of 37.7 psig (2.6 bar gauge), the calculated SFC for the simulation is around 94 g based on the velocity change of a point in the skull facing the shock tube blast (for $\Delta T_{HIC} = 5$ ms).

5.9 Angular Acceleration

Angular acceleration is a major component that can lead to brain injury (King et al. 2003; Weaver et al. 2012; Kleiven 2013; Rowson and Duma 2013). High angular acceleration results in high shear within the brain; injury can arise as a consequence. The calculated initial angular acceleration for the simulation of blasted porcine head is on the order of 10^5 rad/s^2 calculated from the displacement of 2 tracer points at opposite sides of the cranium (mostly around the Y axis). An acceleration of 40,000 rad/s^2 for durations greater than 6.5 ms will have a greater than 99% probability of producing concussion in Rhesus monkeys (whiplash injury on the sagittal plane) (Ommaya et al. 1967). However, since a single point at the cervical spine in the simulation is numerically fixed to the coordinates, the angular acceleration in the simulation is probably overestimated.

A rotational brain injury criterion, $BRIC = \frac{\omega_{max}}{\omega_{cr}} + \frac{\alpha_{max}}{\alpha_{cr}}$, where ω is the rotational velocity and α is acceleration, has been correlated to brain injury—the critical rotation velocity $\omega_{cr} = 42.1$ rad/s and the critical acceleration $\alpha_{cr} = 363$ krad/s^2 for college football data (Weaver 2012; Takhounts et al. 2013). This formula, developed from the Abbreviated Injury Scale data from college football players, could be used as a guide but needs modification to be applicable to blast impact related injury.

It was found that a simple combination of peak change in rotational velocity and HIC showed a high correlation (R = 0.98) with the maximum principal strain in the brain of the National Football League football players (Kleiven 2007).

6. Discussion

6.1 Shear Modulus for the Brain

The shear modulus of human brain tissue has been measured to be 13.0 ± 10 kPa (i.e., from 3 to 23 kPa) for strain rates ranging from 25 to 248 strain/s using the Split Hopkinson Pressure Bar technique (Ott et al. 2012) (Table 5). This range covers many published work on the brain properties (Shuck and Advani 1972; Donnelly 1997; Margulies and Meany 1998; Hamhaber 2006; Kruse et al. 2008; Bilston 2011a; Bilston 2011b; Bayly et al. 2012; Rashid 2012). Among the published works, many use the value 22.53 kPa (Hoberecht 2009; Moore et al. 2009), which is around the upper end of the 13.0 ± 10 kPa mentioned. Since the shear modulus is rate-dependent, the value around the upper end of the 13.0 ± 10 kPa is more appropriate for higher rate problems.

Table 5   Brain material parameters

Density (g/cm^3)	Shear Modulus (bar)	Bulk Modulus (Mbar)	Bulk Sound Speed (cm/µs)	Young's Modulus (kPa)	Poisson Ratio
1.04	0.2253	0.022	0.145	67.6	0.4999

Figure 24 shows the intracranial pressure profile using this shear modulus value of 22.53 kPa instead of 13 kPa (cf. Section 2.2).
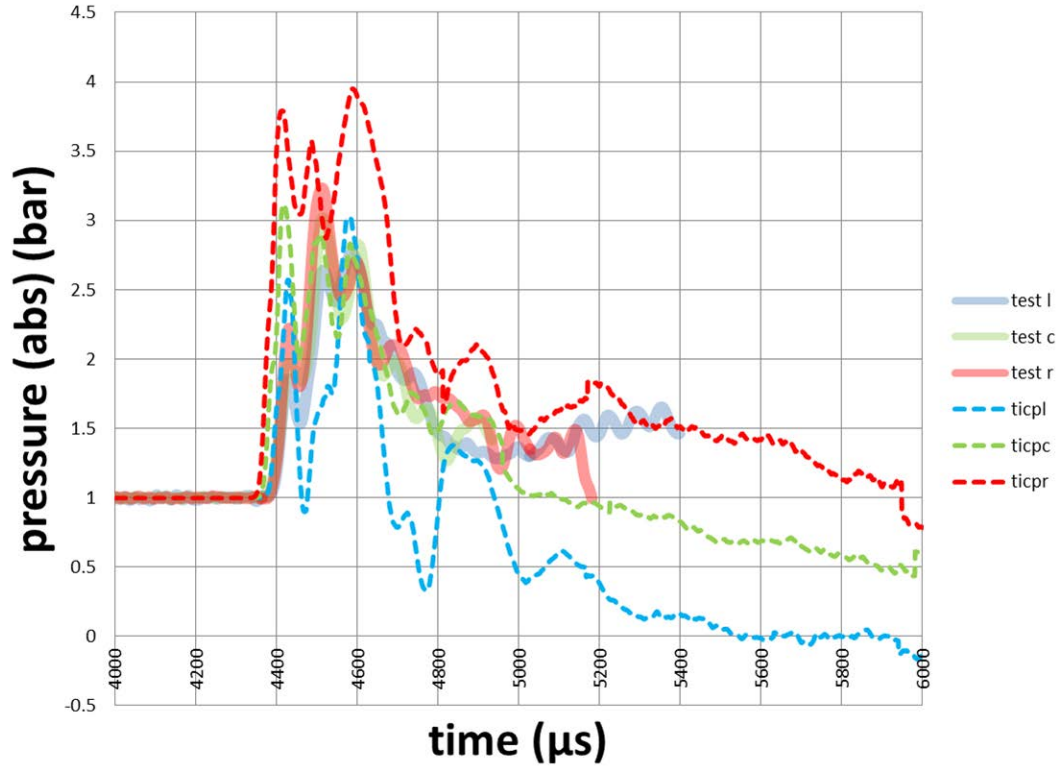
Fig. 24   History of the intracranial pressures where the shear modulus is 22.53 kPa

Since the deviatoric stress is orders of magnitude less than pressure, the shear modulus will have little effect on pressure. So the intracranial pressure measurements will not be sensitive to variations in the shear modulus.

On the other hand, the history of the equivalent strain (mostly shear strain) shows greater sensitivity to the variations in the shear modulus (Fig. 25).
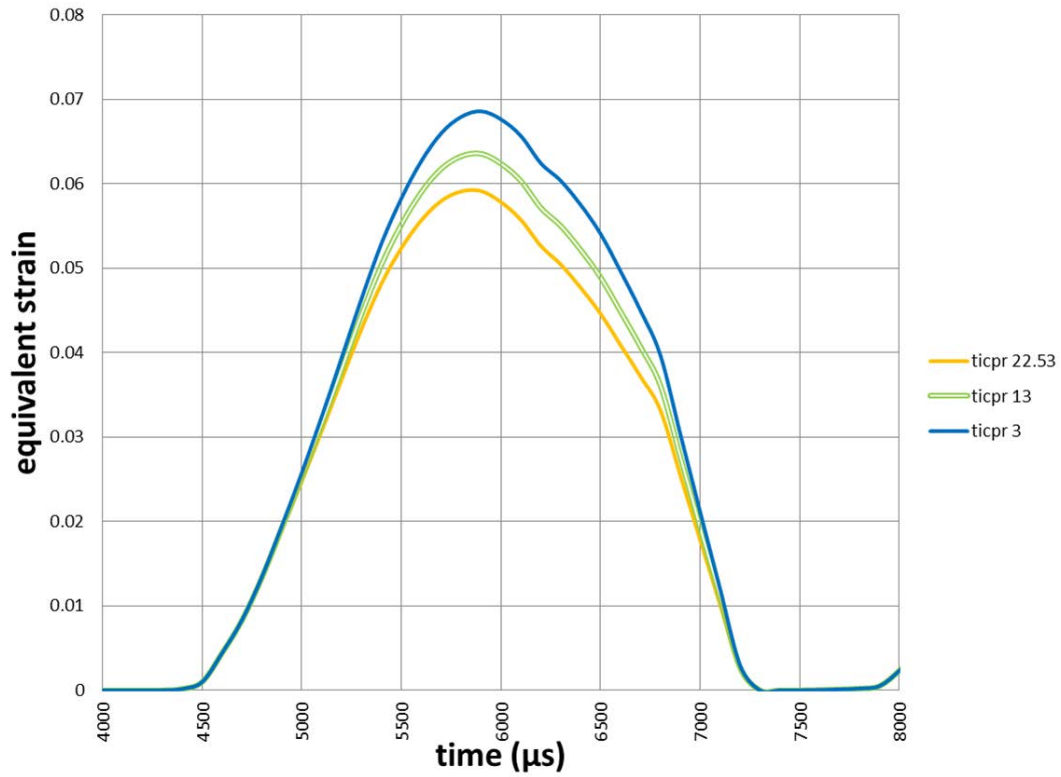
Fig. 25   History of the equivalent strain at the ticpr tracer location for different shear moduli (22.53, 13, 3 kPa)

The history of the von Mises stress (Fig. 26) again shows sensitivity to the variations in the shear modulus.
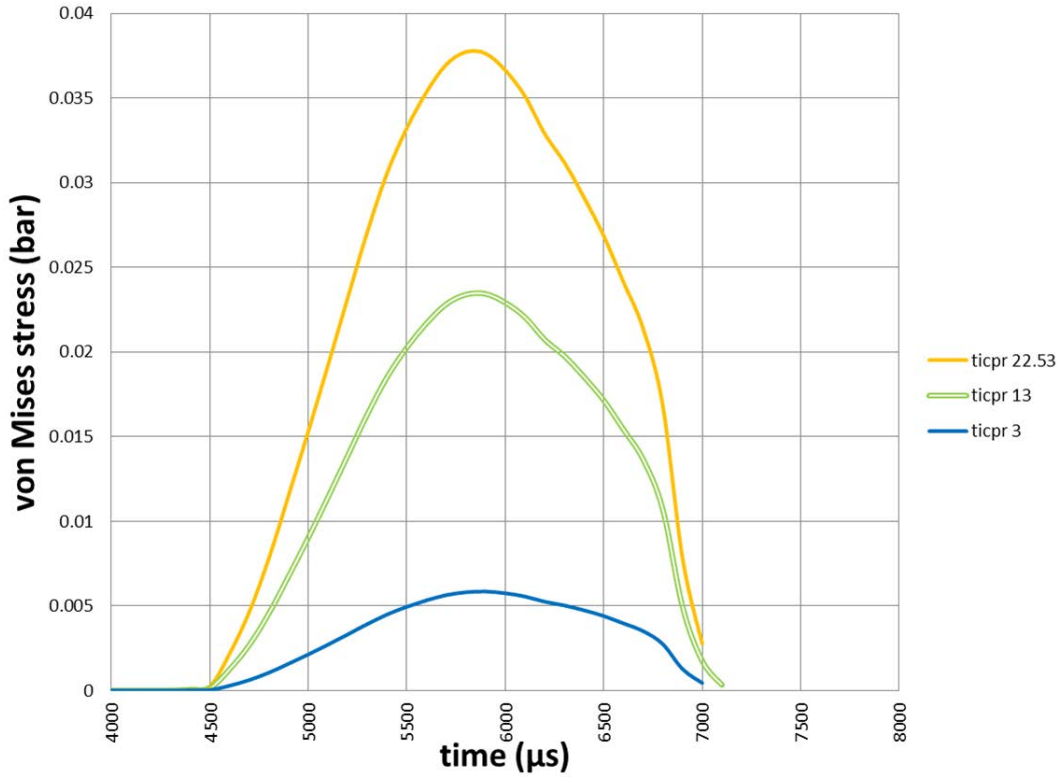
Fig. 26   History of the von Mises stress at the ticpr tracer location for different shear moduli (22.53, 13, 3 kPa).

6.2 The Acceleration of the Head

Figure 27 shows the acceleration of the skull (tracer tac1, equivalent to the accelerometer in the experiments) for different shear moduli. They remain the same. The acceleration in the brain (tracer ticpc; no corresponding measurements) also remain the same for different shear moduli.
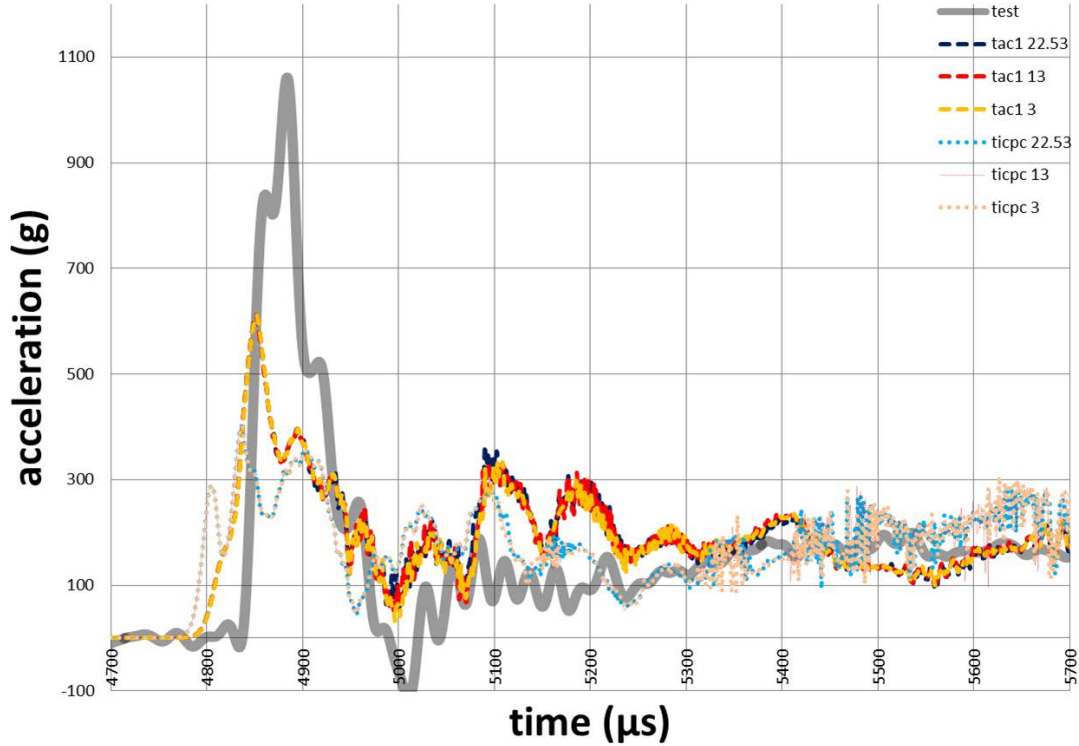
Fig. 27   Acceleration in the head with different shear moduli

6.3 Other Simulation Work Comparison

There have been many attempts to simulate brain injury (Brands et al. 2004; Moore et al. 2009; Nyein et al. 2010; Panzer et al. 2012; Lamy et al. 2013; Zhang et al. 2013; Zhu et al. 2013). In general there were no experimental data on injured human brains to compare. Elaborate partitioning of the brain into functional compartments (gray matter, white matter, corpus callosum, etc.) does not yet have reliable corresponding material properties.

A popular model for brain is the generalized Maxwell model, or simply the viscoelastic model in LS-DYNA (*MAT_VISCOELASIC, *MAT_GENERAL_VISCOELASTIC). The constitutive model for an isotropic viscoelastic material with small strain is given by

$$\sigma = \int_0^t 2G(t - \tau)\frac{d\varepsilon}{d\tau}d\tau + I\int_0^t K(t - \tau)\frac{d\Delta}{d\tau}d\tau \,, \qquad (7)$$

where σ is the Cauchy stress, ε the deviatoric strain, Δ the volumetric strain, I the identity tensor. G(t) and K(t) are the Prony series shear and bulk relaxation kernel functions, respectively.

In a 1-D relaxation test, the Prony series for the shear relaxation is

37

$$G(t) = G_\infty + \sum_{n=1}^{N} G_n e^{-t/\tau_n} , \tag{8}$$

where G_∞ is the long term modulus once the material is fully relaxed and τ is the relaxation time constant. When only one term in the series is used, it can be simplified to

$$G(t) = G_\infty + (G_0 - G_\infty)e^{-t/\tau} , \tag{9}$$

where G_0 is the initial shear modulus independent from relaxation. This is also the form used in LS-DYNA (*MAT_VISCOELASIC). This model works well for some problems. There are various values used for the relaxation time constant in various simulation endeavors. But some simulation work used unrealistic parameters, such as unrealistic time constant. From tests on the rat brain (Finan et al. 2012), the relaxation time constant has been measured to be typically greater than 11 ms, which is far greater than the positive phase of the Friedlander curve of a blast wave. Some simulation work used artificially much shorter time constant. So this model may not have worked well for certain problems.

In the current pursuit using the Mooney-Rivlin model, there is a need to include strain-rate dependency. Since the strain-rate dependency determines the initial peak shear stress after the blast impact, it is critical for the brain injury study. One way to augment the model is to add a strain-rate dependency and a viscoelastic feature to the current Mooney-Rivlin model (2), such as

$$\sigma = \frac{\mu_0}{J}\left[\omega_0\left(\lambda^2 - \frac{1}{\lambda}\right) - (1 - \omega_0)\left(\frac{1}{\lambda^2} - \lambda\right)\right]\left[1 + C \cdot \ln\left(\frac{\dot{\varepsilon}}{\dot{\varepsilon_0}}\right)\right]$$

$$\left[\left(\frac{D}{\mu_0}\right)\int_0^t 2G(t - \tau)\frac{d\varepsilon}{d\tau}d\tau\right], \tag{10}$$

where C is a dimensionless coefficient for the rate dependency, $\dot{\varepsilon_0}$ is a reference strain rate, and D is a dimensionless coefficient for the viscoelastic feature. When fitted to available experimental data, it can provide a more precise peak stress at the moment of impact, which can relate readily to the probability of brain injury.

Figure 28 shows the equivalent strain rate in the porcine brain under blast impact. The maximum strain rate in the brain can reach about 10^4/s (may be mesh resolution dependent). Next to the surface of a penetrating projectile, the equivalent strain rate in gelatin can reach 10^6/s (Huang 2013).
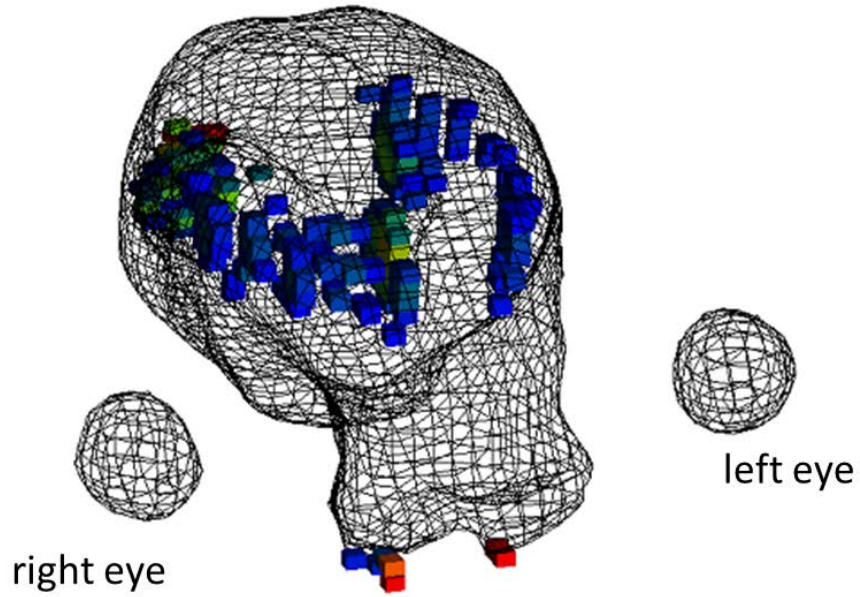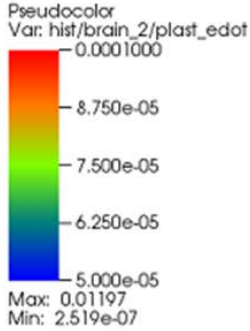
Fig. 28 Region in color at 4,600 μs has the equivalent strain rate in the porcine brain greater than 50/s

In this simulation study there is no viscoelastic relaxation in the model. However, even without the viscoelastic relaxation the intracranial pressure still shows attenuation in time. Furthermore, the viscoelastic shear relaxation tends to lower the probability to brain injury, which makes it somewhat less critical in studying the brain injury when the relaxation time constant is much greater than the positive phase of the blast wave.

39

6.4 Material Properties

Many of the current material property data came from testing with sliced samples. There are sample gripping problems. For instance, in Split Hopkinson Bar tests the samples need to be mounted to the test fixture. Innovative experimental techniques such as shear wave imaging, magnetic resonance elastography are emerging (Mariappan et al. 2010; Macé et al. 2011; Aurant et al. 2012; Bayly et al. 2012; Suzuki et al. 2014; Tomita et al. 2014). Some techniques are noninvasive. They may lead to noninvasive measurement of high strain-rate data of soft tissues in vivo.

In the current simulation study, the skull geometry does not have cavities, and the mesh is not geometry-conforming. The High Intensity Focused Ultrasound and CT can be used to generate more accurate mesh for skull simulation (Aubry et al. 2003; Autuori et al. 2006; Motherway 2009; Nakajima et al. 2009; Binkowski et al. 2010; Kazakia et al. 2013). Meshes having more details of surface outlines, cranial sutures and cranial porosities, and spacial density distribution will greatly enhance the accuracy of simulations, for example, in the bone conduction study.

6.5 Medical Imaging

Continued improvement in imaging techniques may lead to association of minute, initially unidentifiable symptoms with later development of axonal swelling and amyloid and tau protein abnormalities in the brain. These symptoms have also been diagnosed in sportsmen who suffer from chronic traumatic encephalopathy (Makris et al. 2008; Holli et al. 2009; Gavett et al. 2010; MacDonald et al. 2011; Bigler and Maxwell 2012; Goldstein et al. 2012; Lin et al. 2012; MacDonald et al. 2013; Smith et al. 2013; Taber et al. 2013; McKee et al. 2014; Barrio et al. 2015).

6.6 Gender Difference

There are gender differences in the brain, such as in pain thresholds and differential regulation of cell death programs (the anti-inflammatory process of apoptosis and the proinflammatory process of necrosis). XY neurons were more susceptible to nitrosative stress and exhibited a proclivity toward an apoptosis-inducing factor-dependent pathway, while XX neurons were more susceptible to apoptosis-inducing agents (McCarthy et al. 2012; Jog and Caricchio 2013; Ortona et al. 2014; Sharma et al. 2014). Situations may arise where a more precise differentiation in mitigation and treatment between genders for brain injury cases may need attention.

7.   Summary and Conclusion

Shock tube blast on porcine head experimental data, including incident pressure, surface pressure, intracranial pressure, and cranial acceleration, have been compared with simulation using ALE3D. Other physical variables (coup-contrecoup pressure profile, vaporization pressure, skull strain, strain in brain, effective stress, deviatoric strain energy, Löwenhielm vein injury criterion, viscous injury criterion, linear acceleration, and angular acceleration) in the simulations do not have corresponding test data for comparison; they are discussed in association with their injury instigation implications with references to other published findings. The effect of variation of shear modulus based on published measurement data for the brain on impact response is discussed. Furthermore, some nuances about the shock tube simulation are discussed.

With progress in geometry-conforming meshing technique, in noninvasive high-rate properties, and in development in material models, further advances in simulation fidelity will emerge that will help in early diagnosis, treatment, and prevention of brain injury.

8. References

Aerssens J, Boonen S, Lowet G, Dequeker J. Interspecies differences in bone composition, density, and quality: potential implications for in vivo bone research. Endocrinology. 1998;139(2):663–670.

Aubry JF, Tanter M, Pernot M, Thomas JL, Fink M. Experimental demonstration of noninvasive transskull adaptive focusing based on prior computed tomography scans. J Acoust Soc Am. 2003;113(1):84–93.

Aurant ER, Wagner J, Lanning C, Bjugstad KB. Building biocompatible hydrogels for tissue engineering of the brain and spinal cord. J Funct Biomater. 2012;3:839–863.

Autuori B, Bruyère-Garnier K, Morestin F, Brunet M, Verriest JP. Finite element modeling of the head skeleton with a new local quantitative assessment approach. IEEE Transactions on Biomed Eng. 2006;53(5):1225–1232.

Bandak FA, Eppinger RH. A three-dimensional finite element analysis of the human brain under combined rotational and translational accelerations. Warrendale (PA): Society of Automotive Engineers International; 1994. SAE Technical Paper No.: 942215.

Barrio JR, Small GW, Wong KP, Huang SC, Liu J, Merrill DA, Giza CC, Fitzsimmons RP, Omalu B, Bailes J, Kepe V. In vivo characterization of chronic traumatic encephalopathy using [F-18]FDDNP PET brain imaging. Proceedings of the National Academy of Sciences. 2015;112(16):E2039–E2047.

Bass CR, Rafaels KA, Salzar RS. Pulmonary injury risk assessment for short-duration blasts. J Trauma. 2008:65(3):604–615.

Bauman RA, Ling G, Tong L, Januszkiewicz A, Agoston D, Delanerolle N, Kim Y, Ritzel D, Bell R, Ecklund J, Armonda R, Bandak F, Parks S. An intro characterization of a combat-casualty-care relevant swine model of closed head injury resulting from exposure to explosive blast. J Neurotrauma. 2009;26:841–860.

Bayly PV, Clayton EH, Genin GM. Quantitative imaging methods for the development and validation of brain biomechanics models. Annu Rev Biomed Eng. 2012;14:369–396.

Becker R. The new Mooney-Rivlin model, ALE3D manual v4.22. Livermore (CA): Lawrence Livermore National Laboratory (LLNL); 2014.

Bigler ED, Maxwell WL. Neuropathology of mild traumatic brain injury: relationship to neuroimaging findings. Brain Imaging and Behavior. 2012;6:108–136.

Bilston LE. Brain tissue mechanical properties. In: Miller K, editor. Biomechanics of the brain. Berlin (Germany): Springer; 2011a.

Bilston LE. Neural tissue biomechanics. Berlin (Germany): Springer; 2011b.

Binkowski M, Davis GR, Wrobel Z, Goodship AE. Quantitative measurement of the bone density by x-ray micro computed tomography. WCB 2010. In: Lim CT and Goh JCH, editors. IFMBE Proceedings 31; Singapore; 2010 Aug 1–6. Paris (France): International Federation for Medical and Biological Engineering; c2010. p. 856–859.

Bowen IG, Fletcher ER, Richmond DR. Biophysical mechanisms and scaling procedures applicable in assessing responses of the thorax energized by air-blast overpressures or by nonpenetrating missles. Annals of the New York Academy of Sciences. 1968;152(1):122–146.

Brands DWA, Peters GWM, Bovendeerd PHM. Design and numerical implementation of a 3-D non-linear viscoelastic constitutive model for brain tissue during impact. J Biomech. 2004;37:127–134.

Brennen CE. Cavitation and bubble dynamics. New York: Oxford University Press; 1995.

Brennen CE. A review of cavitation uses and problems in medicine. Presented at: Warwick Innovative Manufacturing Research Centre Forum, Warwick University, Coventry, England, 2006.

Bush EC, Allman JM. The scaling of white matter to gray matter in cerebellum and neocortex. Brain Behav Evol. 2003;61:1–5.

Capehart B, Bass D. Review: managing posttraumatic stress disorder in combat veterans with comorbid traumatic brain injury. J Rehabil Res Dev. 2012;49(5):789–812.

Cernak I. Animal models of head trauma. J Am Soc Exp NeuroTheapeutics. 2005;2:410–422.

Champion HR, Holcomb JB, Young LA. Injuries from explosions: physics, biophysics, pathology, and required research focus. J Trauma. 2009;66(5):1468–1477.

Chan P, Lu Z, Rigby P, Takhounts E, Zhang J, Yoganandan N, Pintar F. Development of a generalized linear skull fracture criterion. Washington (DC): National Highway Traffic Safety Administration; 2006. NHTSA Paper No.: 07-0227.

Chatelin S, Deck C, Renard F, Kremer S, Heinrich C, Armspach J, Willinger R. Computation of axonal elongation in head trauma finite element simulation. J Mech Behavior Biomed Materials. 2011;4:1905–1919.

Claessens M, Sauren F, Wismans J. Modeling of the human head under impact conditions: a parametric study. Warrendale (PA): Society of Automotive Engineers International; 1997. SAE Technical Paper No.: 973338.

Courtney E, Courtney A, Courtney M. Shock tube design for high intensity blast waves for laboratory testing of armor and combat materiel. Proceedings of the 28th International Symposium on Ballistics; 2014 Sep 22–26; Atlanta, GA. Lancaster (PA): DEStech Publications, Inc.; c2014. p. 11–14.

Courtney MW, Courtney AC. Working toward exposure thresholds for blast-induced traumatic brain injury: Thoracic and acceleration mechanisms. NeuroImage. 2011;54:S55–S61.

Covey DC, Born CT. Blast injuries: mechanics and wounding patterns. J Surgical Orthopaedic Advances. 2010;19(1):8–12.

Culbert RW. The vapor pressure of human blood by Hill's thermoelectric method. J Biol Chem. 1935;109:547–563.

Dagro AM, McKee PJ, Kraft RH, Zhang TG, Satapathy SS. A preliminary investigation of traumatically induced axonal injury in a three-dimensional (3-D) finite element model (FEM) of the human head during blast-loading. Aberdeen Proving Ground (MD): US Army Research Laboratory (US); 2013. Report No.: ARL-TR-6504. Also available at: http://www.arl.army.mil /arlreports/2013/ARL-TR-6504.pdf.

DePalma RG, Burris DG, Champion HR, Hodgson MJ. Blast injuries. N Engl J Med. 2005;352:1335–42.

Donnelly BR, Medige J. Shear properties of human brain tissue. J Biomech Eng. 1997;119:423–432.

Eppinger R, Sun E, Bandak F, Haffner M, Khaewpong N, Maltese M, Kuppa S, Nguyen T, Takhounts E, Tannous R, Zhang A, Saul R. Development of improved injury criteria for the assessment of advanced automotive restraint

systems - II. Washington (DC): National Highway Traffic Safety Administration; 1999.

Ewing C, Thomas DJ, Beeler GW, Patrick LM, Gillis DB. Dynamic response of the head and neck of the living human to Gx impact acceleration. Warrendale (PA): Society of Automotive Engineers International; 1968. SAE Technical Paper No.: 680792.

Fan WRS. Internal head injury assessment. Warrendale (PA): Society of Automotive Engineers International; 1971. SAE Technical Paper No.: 710870.

Finan JD, Pearson EM, Morrison B. Viscoelastic properties of the rat brain in the horizontal plane. Proceedings of the International Research Council on the Biomechanics of Injury; Dublin, Ireland; 2012 Sep 12–14. [accessed 2015 July 6] http://www.ircobi.org/downloads /irc12/pdf_files/57.pdf.

Finnie JW, Blumbergs PC. Animal models: traumatic brain injury. Vet Pathol. 2002;39:679–689.

Gavett BE, Stern RA, Cantu RC, Nowinski CJ, McKee AC. Mild traumatic brain injury: a risk factor for neurodegeneration. Alzheimer's Research and Therapy. 2010;2:18.

Goldstein LE, Fisher AM, Tagge CA, Zhang X, Velisek L, Sullivan JA, Upreti C, Kracht JM, Ericsson M, Wojnarowicz MW, et al. Chronic traumatic encephalopathy in blast-exposed military veterans and a blast neurotrauma mouse model. Sci Transl Med. 2012;4(134).

Hamhaber U, Sack I, Papazoglou S, Rump J, Klatt D, Braun J. Three-dimensional analysis of shear wave propagation observed by *in vivo* magnetic resonance elastography of the brain. Acta Biomaterialia. 2007;3(1):127–137.

Henry P, Letowski TR. Bone conduction: anatomy, physiology, and communication. Aberdeen Proving Ground (MD): US Army Research Laboratory (US); 2007. Report No.: ARL-TR-4138. Also available at: http://www.arl.army.mil/arlreports/2007/ARL-TR-4138.pdf.

Herbert E, Balibar S, Caupin F. Cavitation pressure in water. Physical Review E. 2006;74:041603.

Hess RL, Weber K, Melvin JW. Review of literature and regulation relating to head impact tolerance and injury criteria. Ann Arbor (MI): University of Michigan; 1980. University of Michigan Report No.: UM-HSRI-80-52-1.

Ho J, Kleiven S. Dynamic response of the brain with vasculature: a three-dimensional computational study. J Biomech. 2007;40:3006–3012.

Ho J, Kleiven S. Can sulci protect the brain from traumatic injury? J Biomech. 2009;42:2074–2080.

Hoberecht RW. A finite volume approach to modeling injury mechanisms of blast-induced traumatic brain injury. [master's thesis]. [Seattle (WA)]: University of Washington; 2009.

Hoge CW, McGurk D, Thomas JL, Cox AL, Engel CC, Castro CA. Mild traumatic brain injury in U.S. Soldiers returning from Iraq. N Eng J Med. 2008;358(5):453–63.

Holli KK, Harrison L, Dastidar P, Wäljas M, Öhman J, Soimakallio S, Eskola H. Texture analysis of corpus callosum in mild traumatic brain injury patients. IFMBE Proceedings. Paris (France): International Federation for Medical and Biological Engineering; 2009.

Huang Y. ALE3D simulation of proximity hit on a long bone in a gelatin block. Aberdeen Proving Ground (MD): US Army Research Laboratory (US); 2013. Report No.: ARL-TR-6426.

Jean A, Nyein MK, Zheng JQ, Moore DF, Joannopoulos JD, Radovitzky R. An animal-to-human scaling law for blast-induced traumatic brain injury risk assessment. Proceedings of the National Academy of Sciences. 2014; 111(43):15310–15315.

Jog NR, Caricchio R. Differential regulation of cell death programs in males and females by poly (ADP-ribose) polymerase-1 and 17β estradiol. Cell Death and Disease. 2013;4(8):e758.

Kazakia GJ, Nirody JA, Bernstein G, Sode M, Burghardt AJ, Majumdar S. Age- and gender-related differences in cortical geometry and microstructure: improved sensitivity by regional analysis. Bone. 2013;52(2):623–631.

Kientzler CF, Arons AB. Vapor pressure of sea salt solutions. Woods Hole (MA): Woods Hole Oceanographic Institution; 1952.

King AI. Fundamentals of impact biomechanics: part I – biomechanics of the head, neck, and thorax. Annu Rev Biomed Eng. 2000.

King AI, Yang KH, Zhang L, Hardy W. Is head injury caused by linear or angular acceleration? Presented at the International Research Council on the Biomechanics of Injury Conference; Lisbon, Portugal, 2003 Sep 25.

Kleinberger M, Sun E, Eppinger R, Kuppa S, Saul R. Development of improved injury criteria for the assessment of advanced automotive restraint systems. Washington (DC): National Highway Traffic Safety Administration; 1998.

Kleinschmit NN. A shock tube technique for blast wave simulation and studies of flow structure interactions in shock tube blast experiments. [thesis]. [Lincoln (NE)]: University of Nebraska, 2011.

Kleiven S. Predictors for traumatic brain injuries evaluated through accident reconstructions. Stapp Car Crash Journal. 2007;51:81–114.

Kleiven S. Why most traumatic brain injuries are not caused by linear acceleration but skull fractures are. Frontiers in Bioeng and Biotech. 2013;1:15.

Kruse SA, Rose GH, Glaser KJ, Manduca A, Felmlee JP. Magnetic resonance elastography of the brain. NeuroImage. 2008;39:231–237.

Lamy M, Baumgartner D, Yoganandan N, Stemper BD, Willinger R. Experimentally validated three-dimensional finite element model of the rat for mild traumatic brain injury. Med Biol Eng Comput. 2013;51:353–365.

Lau IV, Viano DC. The viscous criterion: bases and applications of an injury severity index for soft tissues. Warrenton (PA): Society of Automotive Engineers; 1986. SAE Paper No.: 861882.

Lawrence Livermore National Laboratory (LLNL). User's manual for ALE3D. Livermore (CA): LLNL; 2014.

Lewitus E, Kelava I, Kalinka AT, Tomancak P, Huttner WB. An adaptive threshold in mammalian neocortical evolution. PLOS Biolody. 2014;12(11):e1002000.

Lin AP, Liao HJ, Merugumala SK, Prabhu SP, Meehan WP, Ross BD. Metabolic imaging of mild traumatic brain injury. Brain Imaging and Behavior. 2012;6:208–223.

Ling G, Bandak F, Armonda R, Grant G, Ecklund J. Explosive blast neurotrauma. J Neurotrauma. 2009;26:815–825.

Long, JB, Tong L, Bauman RA, Atkins JL, Januszkiewicz AJ, Riccio C, Gharavi R, Shoge R, Parks S, Ritzel DV, Bentley TB. Blast-induced traumatic brain injury: using a shock tube to recreate a battlefield injury in the laboratory. International Federation for Medical and Biological Engineering Proceedings; 2010.

Löwenhielm P. Dynamic properties of the parasagittal bridging veins. Rechtsmedizin. 1974:55–62.

MacDonald CL, Johnson AM, Cooper D, Nelson EC, Werner NJ, Shimony JS, Snyder AZ, Raichle ME, Witherow JR, Fang R, Flaherty SF, Brody DL.

Detection of blast-related traumatic brain injury in U.S. military personnel. N Engl J Med. 2011;364(22):2091–2100.

MacDonald C, Johnson A, Cooper D, Malone T, Sorrell J, Shimony J, Parsons M, Snyder A, Raichle M, Fang R, Flaherty S, Russell M, Brody DL. Cerebellar white matter abnormalities following primary blast injury in US military personnel. PLOS one. 2013;8(2):e55823.

Macé E, Cohen I, Montaldo G, Miles R, Fink M, Tanter M. *In vivo* mapping of brain elasticity in small animals using shear wave imaging. IEEE Transactions on Medical Imaging. 2011;30(3):550–558.

Makris N, Angelone L, Tulloch S, Sorg S, Kaiser J, Kennedy D, Bonmassar G. MRI-based anatomical model of the human head for specific absorption rate mapping. Med Bio Eng Comput. 2008;46:1239–1251.

Malley WJ. Clinical blood gases: assessment and intervention. Amsterdam (Netherlands): Elsevier; 2005.

Manley GT, Rosenthal G, Lam M, Morabito D, Yan D, Derugin N, Bollen A, Knudson MM, Panter SS. Controlled cortical impact in swine: pathophysiology and biomechanics. San Francisco (CA): University of California-San Francisco; 2005. Report No.: 20050331.

Margulies S, Hicks R. Combination therapies for traumatic brain injury: prospective considerations. J Neurotrauma. 2009;26:925–939.

Margulies SS, Meany DF. Brain tissues. In: Black J, Hastings G, editors. Handbook of biomaterial properties. London (UK): Chapman & Hall; 1998.

Mariappan YK, Glaser KJ, Ehman RL. Magnetic resonance elastography: a review. Clin Anat. 2010;23(5):497–511.

Martin WA. A review of shock tubes and shock tunnels. San Diego (CA): Convair Engineering Department, General Dynamics; 1958. Report No.: ZR-658-050.

Martinez BS. Blast overpressure research program: Kirtland Air Force Base, 1951–1998. San Diego (CA): JAYCOR; 1999.

Maxwell WL, Povlishock JT, Graham DL. A mechanistic analysis of nondisruptive axonal injury: a review. J Neurotrauma. 1997;14(7):419–440.

McCarthy MM, Arnold AR, Ball GF, Blaustein JD, De Vries GJ. Sex differences in the brain: the not so inconvenient truth. J Neuroscience. 2012;32(7):2241–2247.

McElhaney J. Head injury criteria. Polymer Mechanics. 1976;12:411–429.

McElhaney JH, Fogle JL, Melvin JW, Haynes RR, Roberts VL, Alem NM. Mechanical properties of cranial bone. J Biomechanics. 1970;3:495–511.

McKee AC, Daneshvar DH, Alvarez VE, Stein TD. The neuropathology of sport. Acta Neuropathol. 2014;127:29–51.

Moore DF, Jérusalem A, Nyein M, Noels L, Jaffee MS, Radovitzky RA. Computational biology: modeling of primary blast effects on the central nervous system. NeuroImage. 2009;47:T10–T20.

Motherway JA, Verschueren P, Van der Perre G, Vander Sloten J, Gilchrist MD. The mechanical properties of cranial bone: the effect of loading rate and cranial sampling position. J Biomechanics. 2009;42:2129–2135.

Nakajima Y, Uebayashi J, Tamura Y, Matsumoto Y. Large-scale simulation for HIFU treatment to brain. In: Hannemann K, Seiler F. Shock waves: Proceedings of the 26th International Symposium on Shock Waves; Göttingen, Germany; 2009. Berlin (Germany): Springer; c2009. Vol. 2. p. 863–868.

Neal J., Takahashi M, Silva M, Tiao G, Walsh CA, Sheen VL. Insights into the gyrification of developing ferret brain by magnetic resonance imaging. J Anat. 2007;210:66–77.

Needham CE. Blast waves. Berlin (Germany): Springer Verlag; 2010.

Nyein MK, Jason AM, Yu L, Pita CM, Joannopoulos JD, Moore DF, Radovitzky RA. In silico investigation of intracranial blast mitigation with relevance to military traumatic brain injury. Proceedings of the National Academy of Sciences. 2010;107(48):20703–20708.

Ommaya AK, Yarnell P, Hirsch AE, Harris EH. Scaling of experimental data on cerebral concussion in sub-human primates to concussion threshold for man. Warrendale (PA): Society of Automotive Engineers International; 1967. SAE Technical Paper No.: 670906.

Ommaya AK, editor. Head and neck injury criteria: a consensus workshop. Washington (DC): National Highway Traffic Safety Administration (US), Government Printing Office (US); 1981.

Omori K, Zhang L, Yang KH, King AI. Effect of cerebral vasculatures on the mechancial response of brain tissue: a preliminary study. Proceedings of the 2000 ASME International Mechanical Engineering Congress & Exposition. [accessed 2015 July 6] http://www.docstoc.com/docs/139357627/EFFECT-OF-CEREBRAL-VASCULATURES-ON-THE-MECHANCIAL-pdf.

Ortona E, Matarrese P, Malorni W. Taking into account the gender issue in cell death studies. Cell Death and Disease. 2014;5:e1121.

Ott KA, Armiger RS, Wickwire AC, Iwaskiw AS, Merkle AC. Determination of simple shear material properties of the brain at high strain rates. In: Prorok BC, Barthelat F, Korach CS, Grane-Allen J, Lipke E, editors. Mechanics of biological systems and materials, volume 5: proceedings of the 2012 Annual Conference Experimental and Applied Mechanics; Costa Mesa, CA; 2012 June 11–14. Berlin (Germany): Springer; c2012.

Owen-Smith MS. Explosive blast injury. J Roy Army Med Corps. 1979;125:4–16.

Panzer MB, Matthews KA, Yu AW, Morrison B, Meaney DF, Bass CR. A multiscale approach to blast neurotrauma modeling: part I – development of novel test devices for *in vivo* and *in vitro* blast injury models. Frontiers in Neurology. 2012;3. [accessed 2015 July 6] doi: 10.3389/fneur.2012.00046.

Panzer MB, Bass CR, Rafaels KA, Shridharani J, Capehart BP. Primary blast survival and injury risk assessment for repeated blast exposures. J Trauma. 2012;72(2)454–66.

Panzer MB, Myers BS, Capehart BP, Bass CR. Development of a finite element model for blast brain injury and the effects of CSF cavitation. Annals Biomed Eng. 2012;40(7):1530–1544.

Powell BJ, Baumer TG, Passalacqua NV, Wagner CD, Haut RC, Fenton TW, Yang KH. A forensic pathology tool to predict pediatric skull fracture patterns. East Lansing (MI): Michigan State University; 2012.

Rashid B, Destrade M, Gilchrist MD. Mechanical characterization of brain tissue in compression at dynamic strain rates. J Mech Behavior Biomed Materials. 2012;10:23–38.

Reneer DV. Blast-induced brain injury: influence of shockwave components. [dissertation]. [Lexington (KY)]: University of Kentucky; 2012.

Richmond DR, White CS. Biological effects of blast and shock. Albuquerque (NM): Lovelace Foundation for Medical Education and Research; 1966.

Rosenfeld JV, Ford NL. Bomb blast, mild traumatic brain injury and psychiatric morbidity: a review. Int J Care Injured. 2010;41:437–443.

Rowson S, Duma SM. Brain injury prediction: assessing the combined probability of concussion using linear and rotational head acceleration. Annals of Biomedical Engineering. 2013;41(5):873–882.

Sauren AAHJ, Claessens MHA. Finite element modeling of head impact: the second decade. Proceedings of the International IRCOBI Conference on Biomechanics of Impacts; Eidhoven, the Netherlands; 1993 Sep 8–10. p. 241–254. [accessed 09 June 2015]. http://trid.trb.org/view.aspx?id=389940.

Scheidler M, Raftenberg M. Formation of gaps at the specimen-bar interfaces in numerical simulations of compression Hopkinson bar tests on soft, nearly incompressible materials. Aberdeen Proving Ground (MD): US Army Research Laboratory (US); September 2010. Report No.: ARL-TR-5301. Also available at: http://www.arl.army.mil/arlreports/2010/ARL-TR-5301.pdf.

Schreier S. Compressible flow. Hoboken (NJ): John Wiley & Sons; 1982.

Sharma J, Johnson MV, Hossain MA. Sex differences in mitochondrial biogenesis determine neuronal death and survival in response to oxygen glucose deprivation and reoxygenation. BMC Neuroscience. 2014;15:9.

Shridharani JK, Wood GW, Panzer MB, Capehart BP, Nyein MK, Radovitzky RA, Bass CR. Porcine head response to blast. Frontiers in Neurology. 2012;3:70.

Shuck LZ, Advani SH. Rheological response of human brain tissue in shear. J Basic Eng. 1972:905–911.

Smith DH, Hicks R, Povlishock JT. Therapy development for diffuse axonal injury. J Neurotrauma. 2013;30:307–323.

Stuhmiller JH. History of blast injury research. In: A survey of blast injury across the full landscape of military science. New York (NY): NATO Science and Technology Organization; 2011 Oct. Reference No.: RTO-MP-HFM-207.

Suzuki H, Suga M, Fujisaki K, Kajiwara I, Nakamura G, Yoshikawa K, Tadano S. Viscoelastic properties of gel material and soft tissue measured by MRE (magnetic resonance elastography) using micro MRE. International Federation for Medical and Biological Engineering (IFMBE) Proceedings. 2014;43:156–159.

Swindle MM, Makin A, Herron AJ, Clubb FJ, Frazier KS. Swine as models in biomedical research and toxicology testing. Veterinary Pathology. 2012;49(2):344–356.

Taber KH et al. Update on mild traumatic brain injury: neuropathology and structural imaging. J Neuropsychiatry Clin Neurosci. 2013;25(1):1–5.

Takhounts EG, Eppinger RH, Campbell JQ, Tannous RE, Power ED, Shook LS. On the development of the SIMon finite element head model. Stapp Car Crash Journal. 2003;47:107–133.

Takhounts EG, Craig MJ, Moorhouse K, MCFadden J, Hasija V. Development of brain injury criteria (BrIC). Stapp Car Crash Journal. 2013;57:243–266.

Taylor PA, Ford CC. Simulation of blast-induced early-time intracranial wave physics leading to traumatic brain injury. J Biomech Eng. 2009;131:061007.

Terao K. Irreversible phenomena: ignitions, combustion and detonation waves. Berlin (Germany): Springer Verlag; 2007.

Theeler BJ, Erickson JC. Posttraumatic headache in military personnel and veterans of the Iraq and Afghanistan conflicts. Current Treatment Options in Neurology. 2012;14:36–49.

Tomita S, Suzuki H, Kajiwara I, Tadano S, Nakamura G, Jiang Y. MRE simulation based on finite element vibration analysis of viscoelastic model. International Federation for Medical and Biological Engineering Proceedings. 2014;43.

Wang F, Lee HP, Lu C. Effects of head size and morphology on dynamic responses to impact loading. Med Bio Eng Comput. 2007;45:747–757.

Ward C. A head injury model. In: AGARD CP 253: models and analogues for the evaluation of human biodynamic response, performance and protection. Paris (France): Advisory Group for Aerspace Research and Development; 1978. [accessed 09 June 2015]. http://www.dtic.mil.dtic/tr/fulltext/u2/a073811.pdf.

Ward C, Chan M, Nahum A. Intracranial pressure – a brain injury criterion. Warrendale (PA): Society of Automotive Engineers International; 1980. SAE Technical Paper No.: 801304.

Watanabe D, Yuge K, Nishimoto T, Murakami S, Takao H. Development of a human head FE model and impact simulation on the focal brain injury. J Comp Sci & Tech. 2009;3(1):252–263.

Weaver AA, Danelson KA, Stitzel JD. Modeling brain injury response for rotational velocities of varying directions and magnitudes. Annals Biomed Eng. 2012;40(9):2005–2018.

Winter JD, Dornier S, Lukovic J, Fisher JA, St. Lawrence KS, Kassner A. Noninvasive MRI measures of microstructural and cerebrovascular changes during normal swine brain development. Pediatric Research, 2011;69(5):418–424.

Winter J. The material properties of gelatin gels. Aberdeen Proving Ground (MD): US Army Ballistics Research Laboratory (US); 1975. Report No.: BRL Contract Report No.: 217.

Vander Vorst M, Stuhmiller J, Ho K, Statistically and biomechanically based criterion for impact-induced skull fracture. Proceedings of the 47th Annual, Association for the Advancement of Automotive Medicine (AAAM); Lisbon, Portugal; 2003 Sep 22–24. Vermont South, Victoria (Australia): ARRB Group Ltd.; c2003.

Varas JM, Philippens M, Meijer SR, van den Berg AC, Sibma PC, van Bree JLMJ, de Vries DVWM. Physics of IED blast shock tube simulations for mTBI research. Frontiers in Neurology. 2011;2.

Versace J. A review of the severity index. Warrendale (PA): Society of Automotive Engineers International; 1971. SAE Technical Paper No.: 710881.

Viano DC. Biomechanics of head injury – toward a theory linking head dynamic motion, brain tissue deformation and neural trauma. Warrendale (PA): Society of Automotive Engineers International; 1988. SAE Technical Paper No.: 881708.

Wright RM, Ramesh KT. An axonal strain injury criterion for traumatic brain injury. Biomech Model Mechanobiol. 2012;11:245–260.

Zhang L, Yang KH, King AI. A proposed injury threshold for mild traumatic brain injury. J Biomech Eng. 2004;126:226–236.

Zhang L, Yang KH, King AI, Viano DC. A new biomechanical predictor for mild traumatic brain injury – a preliminary finding. Presented at: 2003 Summer Bioengineering Conference; Key Biscayne, FL; 2003 June 25–29. [accessed 09 June 2015]. http://www.tulane.edu/~sbc2003/pdfdocs/0137.pdf.

Zhang L, Makwana R, Sharma S. Brain response to primary blast wave using validated finite element models of human head and advanced combat helmet. Frontiers in Neurology. 2013;4.

Zhang K, Sejnowski TJ. A universal scaling law between gray matter and white matter of cerebral cortex. Proceedings of the National Academy of Science. 2000;97(10):5621–5626.

Zhu F, Chou CC, Yang KH, Wang Z. Numerical simulation of a shock tube for bio-dynamics study. Int J Nonlinear Sci Numer Simul. 2012;13:25–29.

Zhu F, Skelton P, Chou CC, Mao H, Yang KH, King AI. Biomechanical responses of a pig head under blast loading: a computational simulation. Int J Numer Meth Biomed Eng. 2013;29:392–407.

Zilles K, Palomero-Gallagher N, Amunts K. Development of cortical folding during evolution and ontogeny. Trends in Neurosciences. 2013;36(5):275–284.

Zong Z, Lee HP, Lu C. A three-dimensional human head finite element model and power flow in a human head subject to impact loading. J Biomech. 2006;39:284–292.

Appendix.   Shock Tube Simulation

A-1. Effect of Mesh Size

To better understand the simulation of the shock tube, simulations using 2-dimensional (2-D) meshes have been performed. The 2-D meshes here are similar to their 3-dimensional (3-D) counterpart, but the mesh size and configuration have been varied. Figure A-1 shows the pressure history at the center of the shock tube exit for different mesh sizes and configurations as summarized in Table A-1, where rlxginit and rlxweightvar are mesh relaxation parameters in ALE3D. The pressure wave front reached the shock tube exit between 4,600 and 4,700 μs.
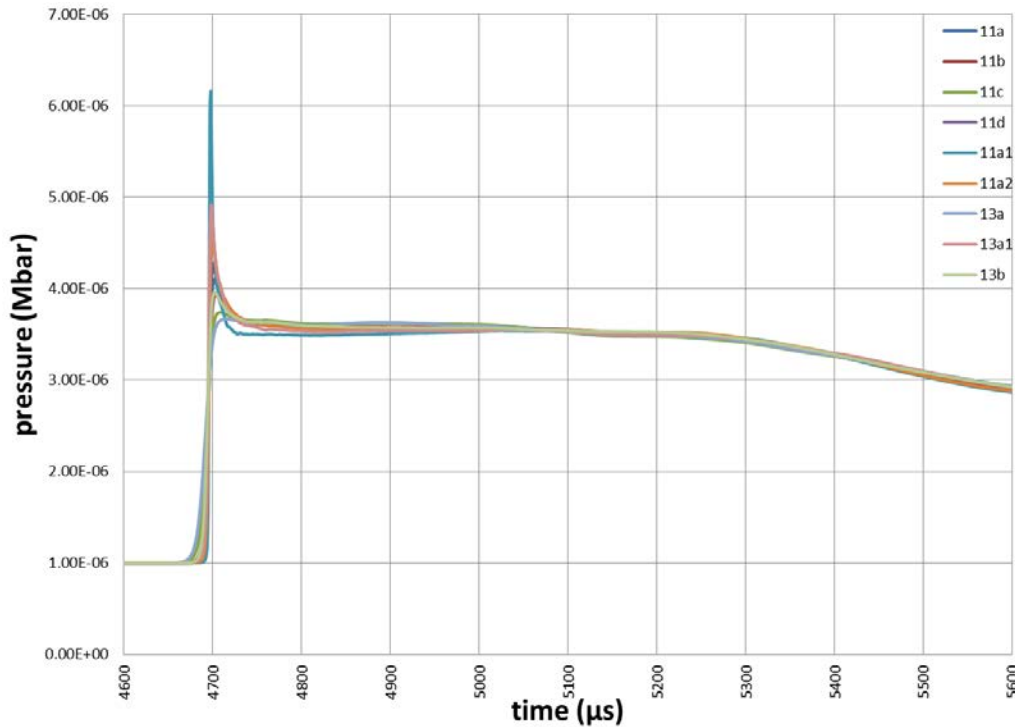

Fig. A-1   Pressure history at the center of the shock tube exit. (The time scale is stretched around the impact time.)

Table A-1   Parameters for Fig. A-1

Label	Initial dx (cm) (end part)	Initial dx (cm) (full tube length)	dx (cm) of the last element at 4,700 μs	rlxginit time (μs)	rlxweightvar
11a	0.5	NA	0.216	4,601	1.e-8
11b	2/3	NA	0.540	4,601	1.e-8
11c	1	NA	0.843	4,601	1.e-8
11d	1/3	NA	0.195	4,601	1.e-8
11a1	0.5	NA	0.012	4,701	1.e-8
11a2	0.5	NA	0.051	4,701	1.e-6
13a	NA	1	0.473	4,601	1.e-8
13a1	NA	1	0.032	4,701	1.e-8
13b	NA	0.5	0.218	4,601	1.e-8

The simulated pressures are all similar, except that with smaller mesh elements the simulation shows higher surge at the time of blast impact, which is likely caused by wave reflection at the mesh boundary where smaller mesh elements are transitioned into larger mesh elements. Figure A-2 shows the pressure profile over the cross section for 3 different mesh configurations (having different dx at 4,700 µs) around the shock wave exit at 4,800 µs. The differences in the pressure profile is effected by the mesh size of the last mesh element where the mesh element size transitions over to a larger mesh size.
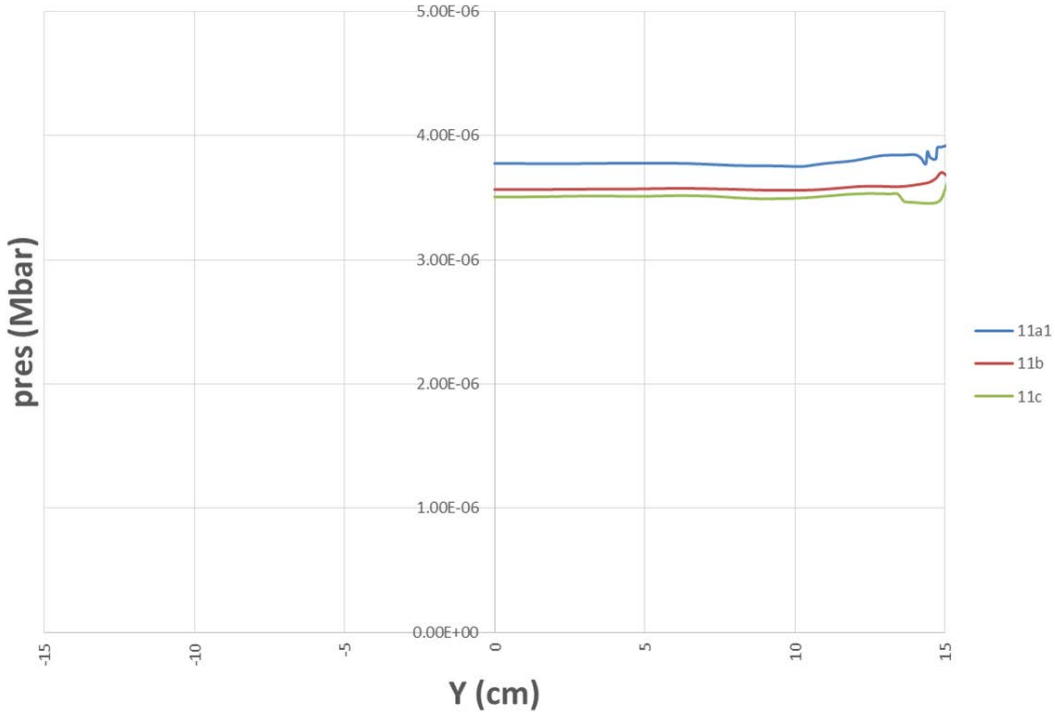

Fig. A-2 **Pressure profile over the cross section for 3 different mesh configurations around the shock wave exit (in 2-D simulation) at 4,800 µs**

A-2. Pressure Profiles within the Shock Tube

In the same 2-D simulation study, the pressure histories at locations along the shock tube direction (X-axis) are plotted as shown in Fig. A-3 (with the parameters in Table A-2). The small wavy patterns in the unloading curves are likely from wave reflections at the discontinuous mesh size transition, which propagates upstream against the subsonic gas flow.
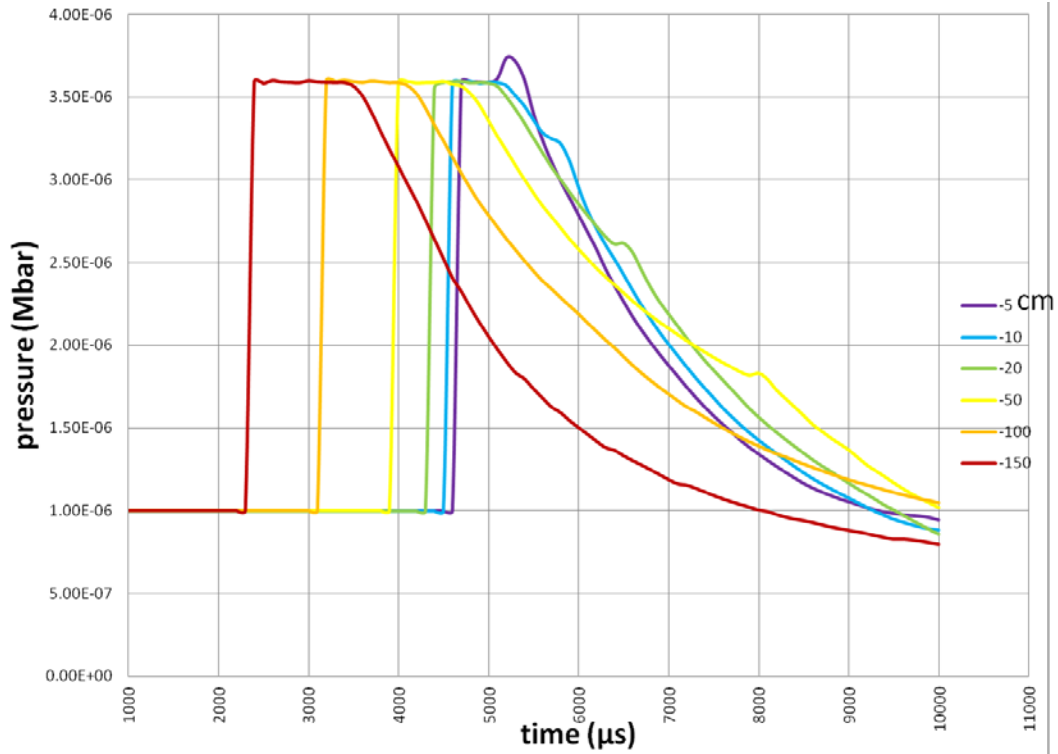
Fig. A-3   Pressure histories at locations along the shock tube near the tube wall

Table A-2   Parameters in the 2-D simulation

Initial dx (cm) (full tube length)	rlxginit time (µs)	rlxweightvar
1	4,601	1.e-8

Figure A-4 shows the pressure histories at similar locations along the centerline of the shock tube.
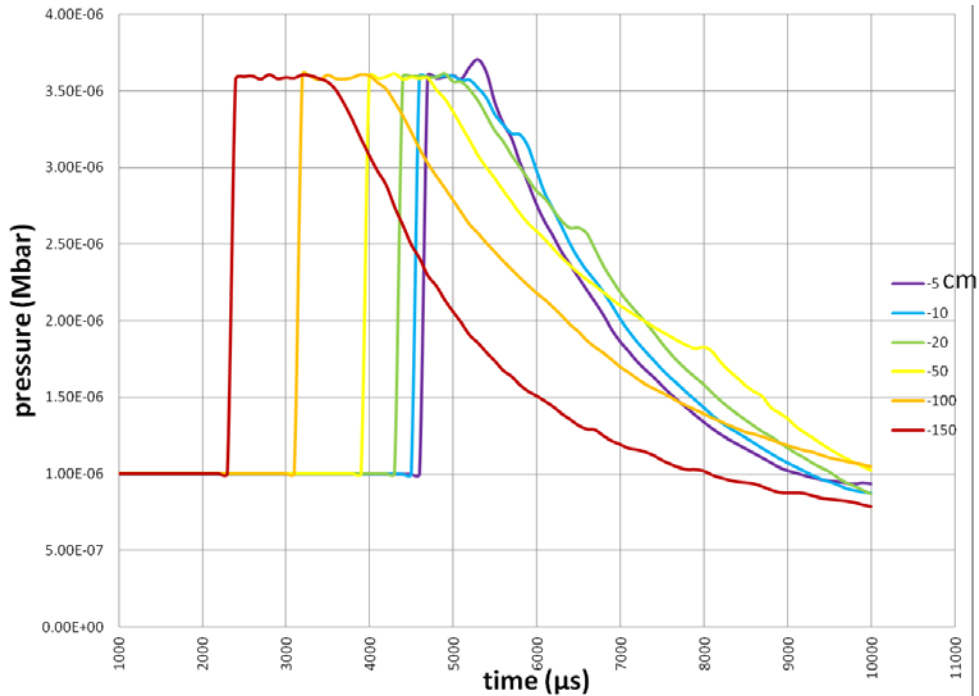
Fig. A-4   Pressure histories at locations along the centerline of the shock tube

There are minimal differences between these 2 figures. The relatively flat top of the curves shrinks with locations toward the exit of the shock tube. Eventually the flat top will reduce to a sharp top when the shock tube is further extended and will resemble a Friedlander wave shape.[1]

Figure A-5 shows the pressure profile next to the centerline of the 3-D shock tube compared with the pressure profile of the 2-D shock tube (3-D parameters detailed in Table A-3). They are very similar. The rarefaction wave (Prandtl-Meyer wave) reflected from the closed backend of the driver section is catching up with the shock wave front. When the length is large enough such that the rarefaction wave is catching up with the shock wave front, the pressure profile will have a narrow top resembling the Friedlander wave form.[2] However, it is not uncommon to find pressure histories with flat top in lab tests.[3,4]

---

[1]Tasissa AF. On the formation of Friedlander waves in a compressed-gas driven shock-tube. [MS thesis]. [Cambridge (MA)]: Massachusetts Institute of Technology; 2014.

[2]Leonardi ADC. An investigation of the biomechanical response from shock wave loading to the head. [Ph.D. thesis]. [Detroit (MI)]: Wayne State University; 2011.

[3]Long, JB, Tong L, Bauman RA, Atkins JL, Januszkiewicz AJ, Riccio C, Gharavi R, Shoge R, Parks S, Ritzel DV, Bentley TB. Blast-induced traumatic brain injury: using a shock tube to recreate a battlefield injury in the laboratory. International Federation for Medical and Biological Engineering Proceedings; 2010;32.

[4]Cernak I, Merkle AC, Koliatsos VE, Bilik JM, Luong QT, Mahota TM, Xu L, Slack N, Windle D, Ahmed FA. The pathobiology of blast injuries and blast-induced neurotrauma as identified using a new experimental model of injury in mice. Neurobiology of Disease. 2011;41:538–551.
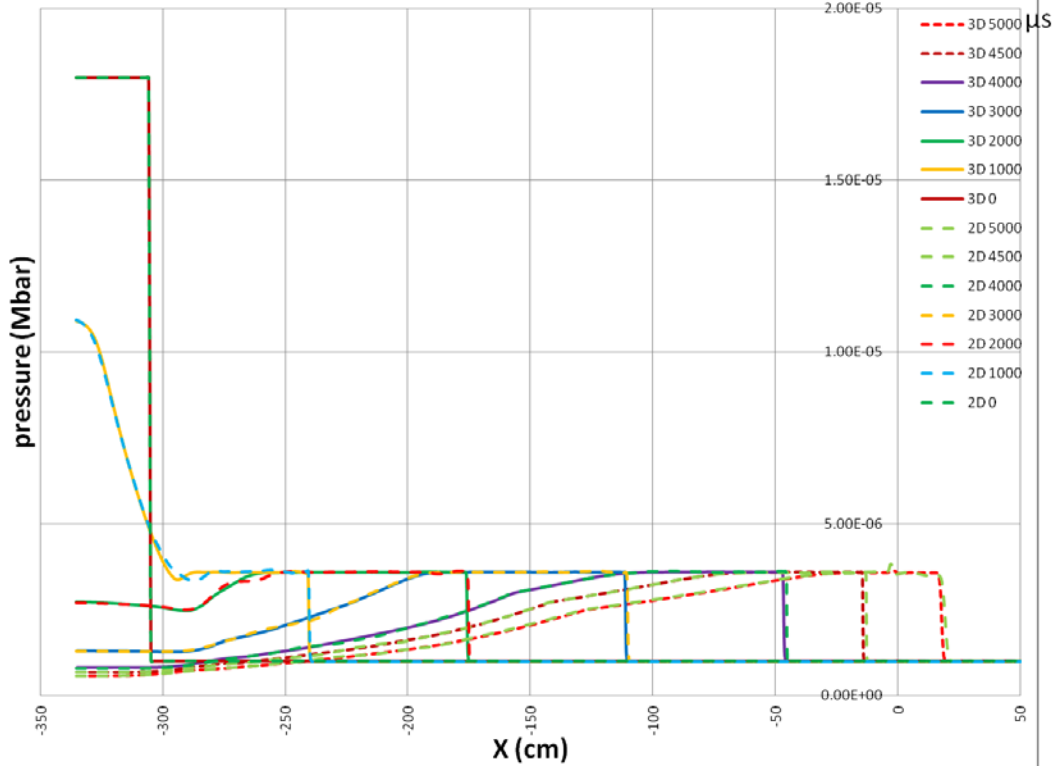
Fig. A-5   Pressure profile along the centerline of the 3-D and 2-D shock tubes at different times

Table A-3   Parameters in the 3-D simulation

initial dx (cm) (full tube length)	rlxginit time (µs)	rlxweightvar
1	4601	1.e-8

Figure A-6 compares the pressure profile next with the tube wall for the 3-D shock tube with the pressure profile for the 2-D shock tube. There is some timing shift. Both profiles show computational problem near the exit of the shock tube.
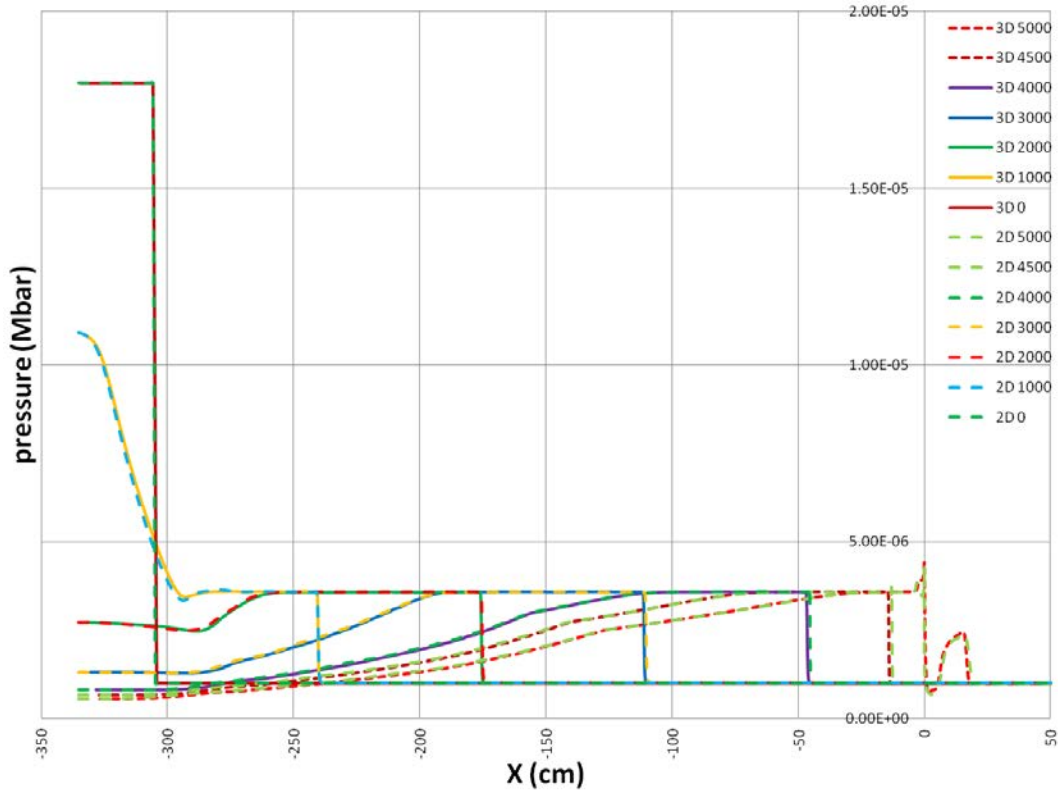
Fig. A-6   Pressure profile next to the tube wall of the 3-D and 2-D shock tubes at different time

A-3. Pressure Profile around the Shock Tube Exit

Figure A-7 shows the pressure profile (in 3-D simulation) around the shock tube exit in elevation plot at 5,500 μs (about 900 μs after the wave front passed the exit). The sharp spikes around the tube end result from higher numerical errors associated with the boundary conditions along the tube wall (cf. Section 4.1 of report). Ignoring the sharp spikes, the profile shows a nonplanar pressure distribution over the cross section having higher pressure near the centerline and lower pressure closer to the tube wall. The small pressure rise near the pressure front (around $X = 40$) comes from mesh transition from fine mesh to coarse mesh (from small dx to large dx).

61
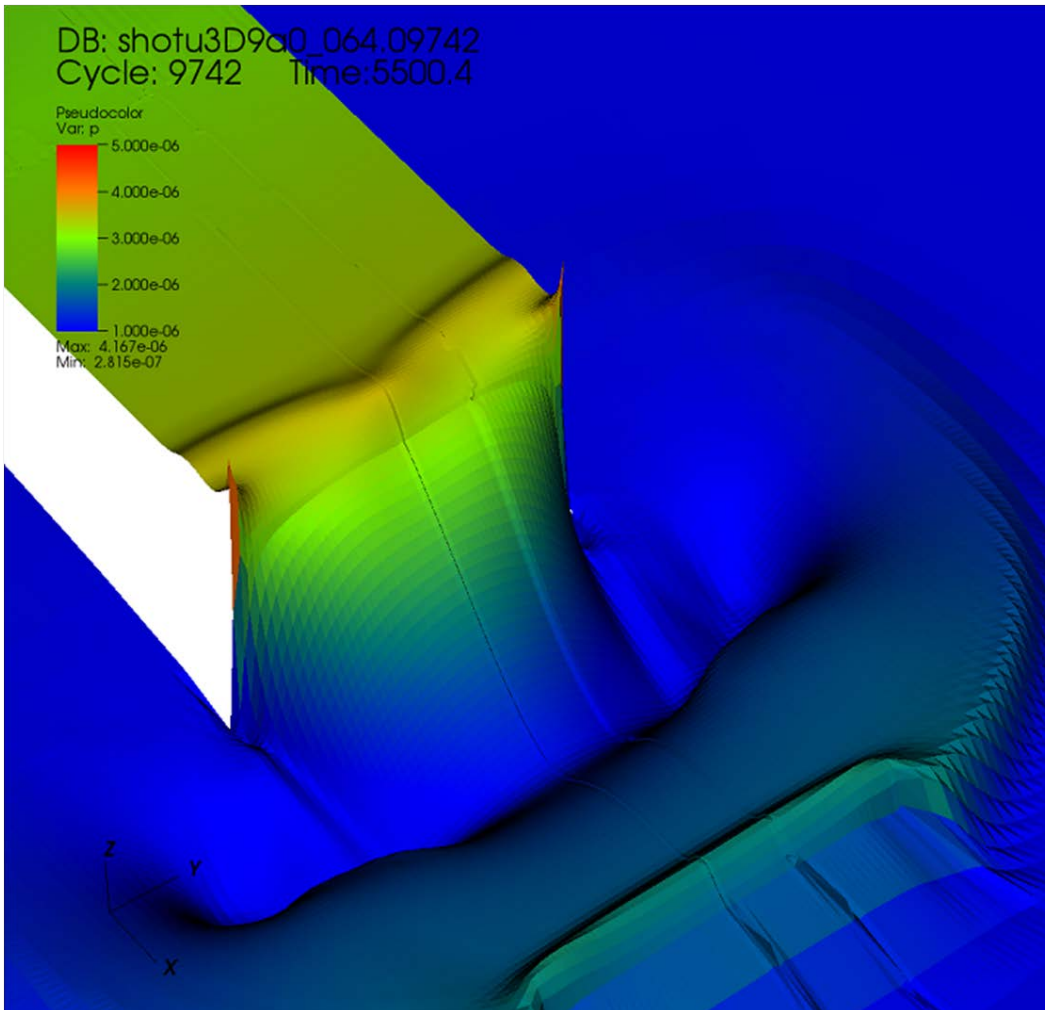
Fig. A-7   Pressure profile at 5,500 μs around the shock tube exit in elevation plot

Figure A-8 shows the pressure profile over the cross section for 3 different times around the shock wave exit (in 3-D simulation). Solid lines are sampled at location 5 cm upstream from the exit; dashed lines are sampled at the exit (the pressure transducer locations). Ignoring the numerically erroneous higher values near the wall, the pressure around the centerline is higher than the pressure toward the tube wall.
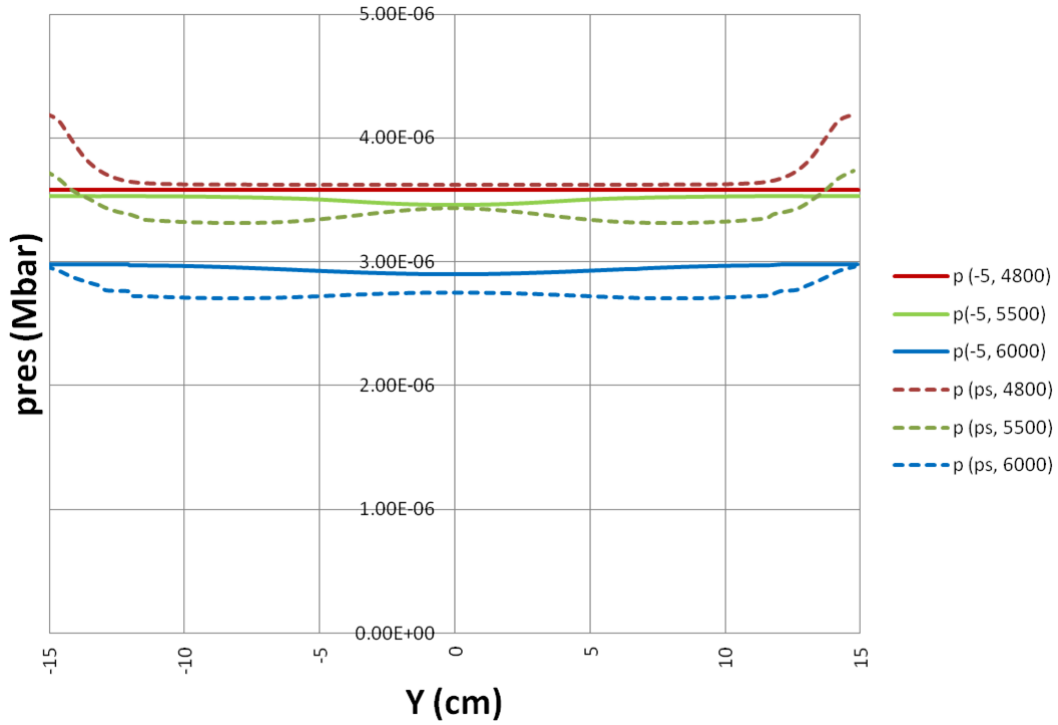
Fig. A-8   Pressure profile over the cross section for 3 different time around the shock wave exit (in 3-D simulation)

Figure A-9 shows the difference in the pressure profiles at exit between the 3-D and the 2-D simulations. Because there is a small timing shift coming from mesh differences in the shock tube, the time selected for 2-D lines is a little shifted from that in 3-D in order to find a closer match. The differences in pressure near the tube wall may come from differences in the mesh resolution and in the relaxation processes.
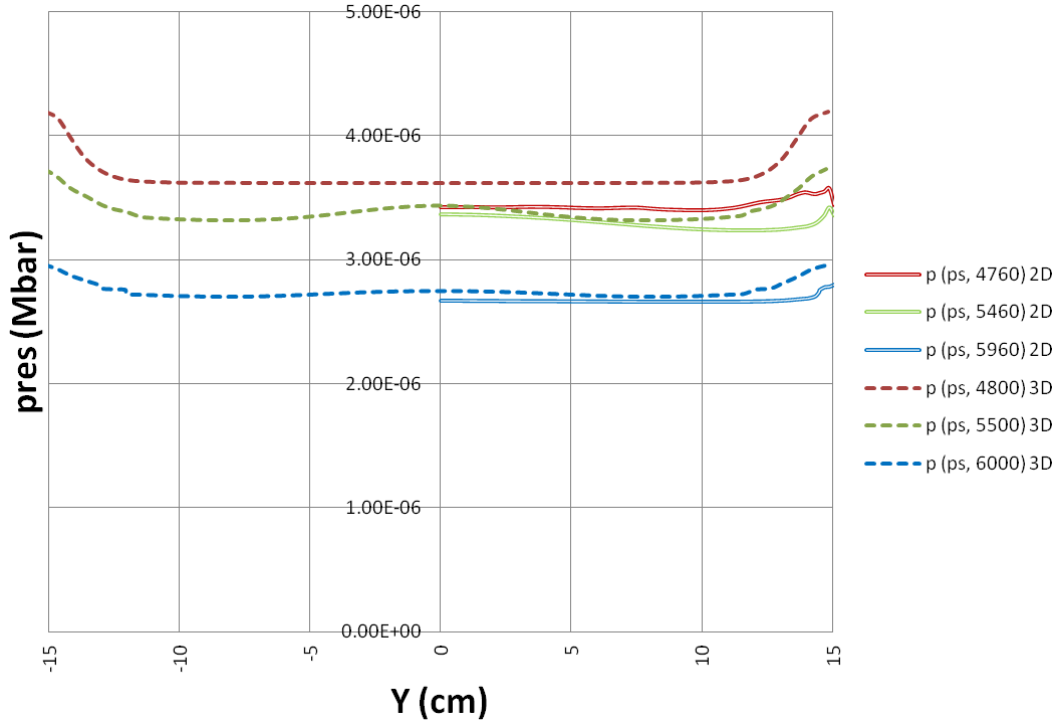
Fig. A-9   Difference in the pressure profiles between the 3-D and the 2-D simulations

From the simulated pressure profile with planar pressure wave, and the fact that in experiments the initial pressure wave is a jet through the Mylar diaphragm, the pressure at the center of the shock exit will be higher than the pressure near the wall.

List of Symbols, Abbreviations, and Acronyms

1-D	1 dimensional
2-D	2 dimensional
3-D	3 dimensional
CSF	cerebro-spinal fluid
CT	computed tomography
HIC	head injury criterion
MSC	mean strain criterion
SFC	skull fracture correlate
TBI	traumatic brain injury